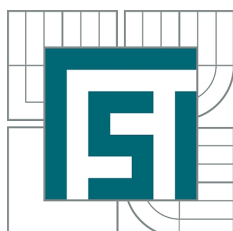# BRNO UNIVERSITY OF TECHNOLOGY
VYSOKÉ UČENÍ TECHNICKÉ V BRNĚ

FACULTY OF MECHANICAL ENGINEERING
INSTITUTE OF PHYSICAL ENGINEERING

FAKULTA STROJNíHO INŽENÝRSTVí
ÚSTAV FYZIKÁLNíHO INŽENÝRSTVí

SURFACE PLASMON RESONANCES ON COLLOIDAL NANOPARTICLES
POVRCHOVÉ PLAZMONOVÉ REZONANCE NA KOLOIDNíCH NANOČÁSTICíCH

MASTER'S THESIS
DIPLOMOVÁ PRÁCE

AUTHOR   Bc. JIŘí BERÁNEK
AUTOR PRÁCE

SUPERVISOR   prof. RNDr. TOMÁŠ ŠIKOLA, CSc.
VEDOUCÍ PRÁCE

BRNO 2013

Summary

The presented diploma thesis is focused on the Localized Surface Plasmons (LSP). The far-field optical response of the colloidal solutions of gold nanoparticles caused by LSP was investigated and compared with the numerical calculations. For the simulations, the Discrete Dipole Approximation (DDA) and Finite-Difference Time Domain (FDTD) techniques were employed. In particular, the shape and size effects of spherical particles and nanorods were studied. The simulations performed by both methods are in a good agreement for the spheres. For the nanorods, the resonance was found to be affected markedly by their geometry. Also, broader resonance peaks were found. This effect was assigned to the sample size distribution and its influence is discussed by comparing the simulations with experiments. In addition, synthesis of nanorods was carried out as well. Finally, the results on the study of optical properties of silver clusters formed under equilibrium conditions are presented.

Abstrakt

Předkládaná diplomová práce se zabývá lokalizovanými povrchovými plazmony (LSP) na koloidních nanočásticích. Byla provedena experimentální měření a teoretické simulace odezvy nanočástic v dalekém poli způsobené těmito plazmony. Pro simulace jsme použili metodu metodu diskrétní dipólové aproximace (DDA) a metodu konečných prvků v časové doméně (FDTD). Výzkum byl zaměřen na vliv tvaru a velikosti nanočástic, zejména sférických nanočástic a nanotyčinek. Zkoumali jsme vlastnosti sférických nanočástic a nanotyček. Simulace se dobře shodují s experimenty v případě kuliček. V případě tyčinek jsme pozorovali závislost polohy rezonance na tvaru tyčinky. Rozšíření rezonančních píků je přisouzeno většímu rozptylu geometrických parametrů nanočástic a diskutováno na základě srovnání experimentálních dat a výpočtů.V rámci experimentů byla rovněž provedena syntéza zlatých nanotyčinek. Poslední částí práce je studie optických vlastností stříbrných nanočástic. Pomocí diskrétní dipólové aproximace jsme simulovali vliv rovnovážného tvaru na optickou odezvu.

Keywords

Plasmonics, Localized Surface Plasmons, Gold, Nanoparticles, Colloids, DDA, FDTD

Klíčová slova

Plazmonika, Lokalizované povrchové plazmony, zlato, nanočástice, koloidní roztoky, DDA, FDTD

I hereby declare that I elaborated this thesis independently under the supervision of prof. RNDr. Tomáš Šikola, CSc. and solely with the support of the listed literature.

Bc. Jiří Beránek

Contents

CONTENTS

4

Chapter 1

Introduction

At present, colloidal nanoparticles are an indispensable ingredient in the development of sophisticated ways of diagnosis, sensing or treatment [1]. They are of great interest in the field of solar cell research [2, 3] and energy storing [4]. The catalytic effects are important for chemical applications, as the nanoparticles can replace organic solvents [5]. In applied science, gold nanoparticles are useful in electron microscopy for their high electron density, giving excellent contrast in the micrographs. On the other hand, gold is often used in experimental biochemistry for labeling macromolecules as oligonucleotides or entire DNA, exploiting photoluminiscence [6], Raman spectroscopy [7] or other techniques for their detection. In this scope, nanoparticles offer an alternative to chemical dyes or work as their complementaries to enhance the sensitivity of present techniques for chemical analysis.

However, the effects of nanoparticles, which we can explain and modify to our purposes nowadays, were utilised in the work of man much earlier. Probably, the most famous is the Lycurgus cup, a piece of the 4th century Roman craftwork. It is an example of a dichroic glass. Such a type of glass changes its color when observed in transmitted and scattered light, see Freestone [8]. Stained glass used in the vitrails gets its red, or ruby red color, in the similar way, as the light transmitted through it interacts with metallic nanoparticles, see Figure 1.1.

Figure 1.1: The Lycurgus cup. Jade color is observed with the illumination from outside, red color appears when the source of light is placed inside the cup. On the right, we see the vitrail from the cathedral of Saint-Étienne de Bourges. The glass tables were dyed by adding substances which formed gold nanoparticles in the glass. Source: *site.dreamsofglass.com* and *http://www2.ac-lyon.fr*.

The theory of electrodynamics has opened the way to explain optical properties of nanoparticles dispersed in ambient medium. Of particular interest were the colloidal solutions where the effect of varying the diameter of particles on the color of the solution was clearly demonstrated. This behavior was explained in 1908 in Gustav Mie's work [9], which has been highly recognized until nowadays for its completeness and clarity.

Ultimately, it was the progress in nanotechnology and state-of-the-art techniques for observing and manipulating objects on the nanoscale, that put nanoparticles together with the entire palette of nanostructures, in the light of an active interest of scientists and engineers. One of the main problems encountered in nanotechnology is often limited possibility to produce the structures of required properties at a reasonable efficiency, setting a borderline between the applicable and inapplicable discovery. In case of nanoclusters, this limit has been overcome by synthesis methods, see Section 5.3, providing us with samples of well-defined properties. Current possibilities are opening the scope for both theoretical and experimental investigations that can fully utilize the properties of nanoparticles towards above-mentioned applications.

In the presented work, we investigate the optical properties of noble metal nanoparticles in colloidal solutions, both experimentally and theoretically. The theory explaining scattering effects, and the way to quantify them, is given in Chapter 2 together with an outline of the Mie solution. The influence of the dielectric function and geometry is discussed in Chapter 3. As the final part of the theoretical background, Chapter 4 is devoted to the description of main aspects of employed numerical methods.

Chapter 5 covers the experimental part of the work. The first measurements were done on the samples containing spherical particles. Such a kind of samples represents an ideal way to test the optical apparatus because the spectra can be accurately predicted by the Mie theory. Moreover, knowing the Mie solution, we can test the accuracy of prediction made by approximative numerical techniques. Further, optical spectra were measured on the samples of gold nanorods. These results are compared with the numerical calculations and the experiments represent the first step towards nanoparticle synthesis at the Institute of Physical Engineering. The last section of Chapter 5 presents a systematic study of optical properties of silver nanoclusters with the focus on the effect of their shape on the optical spectra and color of comprised colloidal solution.

Chapter 2

Scattering

Many objects around us do not radiate light themselves. They are visible to us thanks to the light from different sources that is reflected, or generally speaking, scattered by their surface. Scattering is one of the basic concepts in the interaction of light and matter and it is manifested frequently in our everyday life. We can find many examples of scattering in the atmosphere. Colors that appear on the sky during the daytime is the effect of scattering of the sunlight by atmospheric particles. The cream-white color of the Milky Way is the light of the stars from our galaxy scattered by interstellar dust. Scattering appears also when there is a fluctuation of concentration of the particles dispersed in some media or when there is a change of their orientation if they are anisotropic. We can expect that the light will be scattered when it propagates through heterogeneous media. Therefore, strictly taken, only the perfect vacuum is the medium which can be considered homogeneous.

We can come across the term scattering in another fields like acoustics or quantum mechanics. We restrict our attention to the realm of electromagnetism where we can define scattering as follows [10]:

> Scattering of the electromagnetic radiation is a process of interaction with the heterogeneity of the guiding media (solid, gas or liquid) that results in the change of properties of primary beam in sense of its direction of propagation, phase, polarization or wavelength.

Electromagnetic field, acting on the particle, forces the electrons in its atoms to oscillate. This oscillatory motion is not constant in terms of acceleration, therefore electrons emit radiation. In the terms of quantum mechanical processes it is the excitation of the electron to higher energy levels followed by emission of a energy quantum. If the energy of the emitted photon is the same as the energy of the absorbed one, we refer to it as the elastic scattering. If the energies of these two photons are different, we say that the scattering is inelastic. The inelastic scattering is used in Raman spectroscopy.

The process of scattering, which we schematically depicted in Figure 2.1, consists of absorption of light and subsequent reradiation. We do not consider the processes belonging to luminiscence here, i.e. the processes with a measurable delay between illumination and reradiation. The reradiated light is called the scattered light. The light which passes unchanged is called transmitted and the light which is lost in the interaction with the atoms of the particle is called the absorbed light. Scattering, as outlined above, is an underlying physical process to many effects like the diffraction, refraction of light or specular
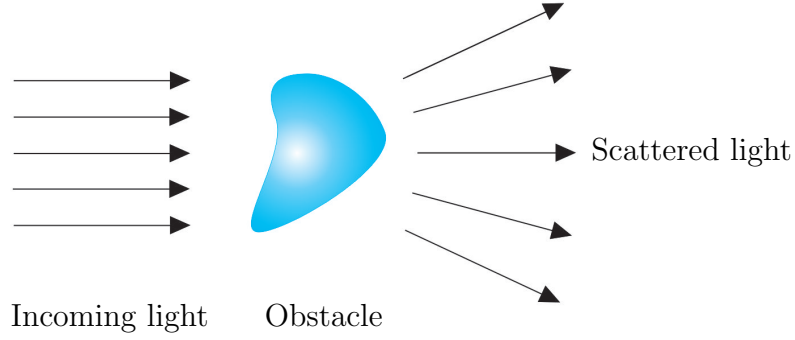
Figure 2.1: Light scattered by a particle.

reflection. For example, the light incident on a glass interface undergoes a refraction by the Snell's law. But microscopically, it is still the light interaction with individual atoms, and the light produced by them, which are responsible for the extinguishing of primary beam. By the constructive interference of the secondary radiation, the refracted beam appears in the direction predicted by the law of Snell.

The two probably most recognized physicists in the field of scattering of electromagnetic waves are lord Rayleigh and Gustav Mie.

Rayleigh developed theory of interaction of light with particles that are nonabsorbing, i.e. dielectric, and much smaller than the wavelength of visible light. He examined the intensities of scattered and incoming light considering the volume of scattering particles V, distance between the particle and the point of observation r and wavelength λ. By simple and straight argumentation [11], he concluded that particles scatter light with the intensity inversely proportional to the fourth power of the wavelength of incoming light. The equation for Rayleigh's scattering is

$$I = I_0 \; \frac{(2\pi)^4}{r^2\lambda^4} \; VN\alpha^2(1+\cos^2\vartheta), \tag{2.1}$$

where N is the concentration of particles in the sample and ϑ is the angle in the scattering plane. The scattering plane is defined as a plane where both the incoming and the scattered rays lie. We can see from equation (2.1) that the intensity of scattered light is higher for shorter wavelengths. Thus the most commonly observed example of the Rayleigh scattering is the blue color of the sky.

Explanation of the interaction of the light with spherical objects with the size comparable or greater than the wavelength of light was done in 1908 when the German physicist Gustav Mie published his work on this topic [9]. By that time the solution of Maxwell's equations was already known. Mie worked with the known methodology and developed numerical technique to find the important scattering constants. The result itself does not provide much insight, as it is in the form of infinite series, but it is convenient for computer simulations. The theory presented by Mie is more general than Rayleigh's conclusions and for the increasing radius its results converge to the geometrical optics. The example of the Mie scattering is also readily found in the atmosphere. Particles of water or ice crystals accumulated in clouds have sizes of approximately 10 μm. Such particles scatter light without any strong dependence on wavelength. Thus the clouds seem white to us.

8

In the presented theory, we follow the concept and methodology of the explanation given by Bohren and Huffman [12]

To explain completely the scattering, we must consider the elemental structure of matter. The strict approach would employ quantum mechanics, but we are usually not interested in processes taking place in individual atoms. We are interested in the overall effect of the entire object. So we stay with a more general explanation. Our task can be formulated in the following way [12].

> Consider a particle of a given material, dimensions and shape, embedded in a nonabsorbing, isotropic and homogeneous medium. The particle is acted upon by an external harmonic time-dependent electromagnetic field of certain frequency or an interval of frequencies. For each point within or outside the particle, find the local electromagnetic field given by the superposition of the incident field and field induced by the particle itself.

The classical explanation of the process which leads to scattering considers the object as a system consisting of positive lattice atoms with electrons bound to the atoms by spring-like force. The electromagnetic wave provides a driving force that makes the electrons oscillate. The oscillatory motion of electrons results in emition of the radiation. In the quantum mechanical point of view, the action of electromagnetic field is represented by a photon which, when absorbed in an atom, excites an electron to a level with higher energy. When the electron falls to a lower energy level, it is generally with the emission of a photon. Both approaches include excitation by radiation and subsequent emission of secondary radiation (i.e. re-radiation).

$$\text{Scattering} = \text{Excitation} + \text{Reradiation} \tag{2.2}$$

If there are more sources of electomagnetic field, we have to sum their contributions according to the principle of superposition to get the resultant field. The sum of the field of the induced dipole and the external field create an effective field, which again acts upon the dipole. We can imagine the particle to consist of many such dipoles - the approximation suitable for the mathematical treatment, as we shall see later. To get the net force, we must consider the mutual interaction between all the dipoles or at least in the distance where their influence cannot be omitted. Therefore with this point of view, we arrived to the electromagnetic many-body problem which, to add to the complexity, is self-consistent.

However, the concept of dividing the particle into subvolumes to which we can assign a certain dipole moment gives us an opportunity to infer some qualitative results.

We consider the elastic scattering and suppose that the dimensions and shape of the particle are arbitrary. We divide the volume of the particle into subvolumes, as schematically depicted in Figure 2.2. In each subvolume, there is one electric dipole which radiates light in all directions. To measure the intensity of electromagnetic field, we use a converging lens which directs only the light of a certain direction to its focal point, here labeled as D, where we place our detector. The measured intensity will be a sum over contributions of all the dipoles. As the particle represents a coherent source of radiation, the phase difference will be the most important factor.
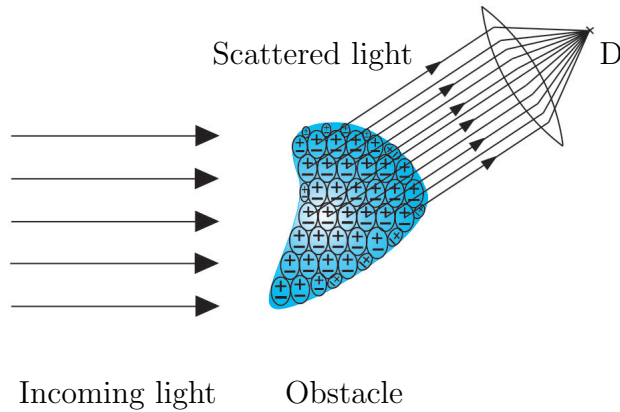
Figure 2.2: Light scattered into a particular direction. Intensity measured at the point D generally varies with direction.

When the particle is much smaller than the wavelength of the incoming light, we can expect that all the dipoles will be in phase and there will be a little dependence of intensity on the position of the point D. As the size of the particle increases, there is higher probability that the field acting on the particle will be different over its volume and the dipoles will be phase-shifted. Thus the dependence of the intensity on the position of the detector will reveal more complicated behavior with generally more minima and maxima.

The amplitude of the scattered light is only a function of the material described by the complex dielectric function. The dielectric function fully specifies the behavior of the considered material in the electric field. A closer look at this property is taken in Section 3.2.

In the real experiment, it is common that we do not measure the optical response of a single particle. However, such a measurement can be done, for instance, using the technique of optical tweezers in a liquid medium, but there is a problem of a very small relative intensity of the scattered light. More accessible is the measurement of a large amount of particles dispersed in a certain medium over its volume. In principle, such a system can be treated with a similar methodology as mentioned above. There is no more complexity as long as the particles are mutually separated in the solution over such average distances that their fields do not interact with each other. We will consider this "dilute regime" throughout our study. However, the non-diluted regime possesses some interesting applications [13].

From the nature of scattering we can expect energy-dissipating processes leading to the damping of the oscillatory motion of electrons. One form of damping can transfer the energy associated with electron oscillations into the heat. Absorption and scattering always occur simultaneously and are inherently connected to each other.

2.1. Scattering and absorption cross section

The rate at which energy is transferred by the beam of light can be expressed by the output P. This quantity is easy to measure by a suitable detector and we can use it for the description of the transmission of the light through heterogeneous media. If we place the detector into the path of the light beam, we can measure its intensity and thus get an output P_0. Then we put a sample, for instance a solution with particles, between the light source and the detector, and we get an output P, where $P < P_0$. The loss of energy is caused by the sum of absorption and scattering, and is generally called the extinction.
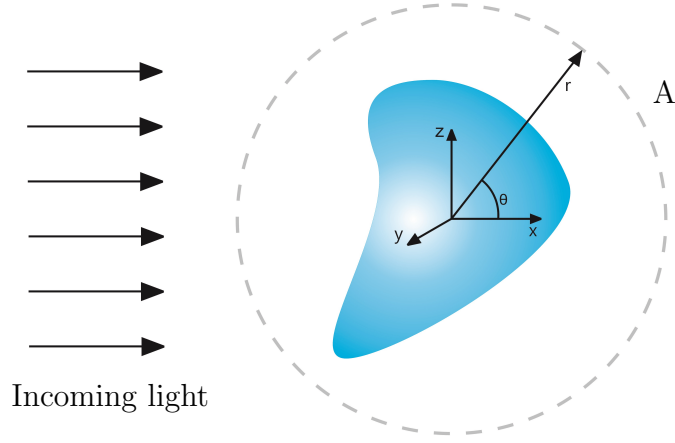

Figure 2.3: Spherical surface surrounding the particle.

For the quantitative description of the extinction of light by a particle we must first examine the flux of the Poynting vector $\mathbf{S}$ through the sphere surrounding the object, see Figure 2.3. The rate of transmission of energy through the enclosed sphere surface A can be written as

$$W_a = -\int_A \mathbf{S} \cdot \mathbf{e}_r \mathrm{dA} \tag{2.3}$$

The relation (2.3) includes the negative integral to provide that the energy entering the enclosed space is positive and the energy leaving this space is negative. We see that W_a directly expresses the rate at which particles absorb light. It is always non-negative and can be written as the sum of three parts

$$W_a = W_i - W_s + W_{ext}, \tag{2.4}$$

where

$$W_i = -\int_A \mathbf{S}_i \cdot \mathbf{e}_r \mathrm{d}A, \qquad W_s = -\int_A \mathbf{S}_s \cdot \mathbf{e}_r \mathrm{d}A, \qquad W_{ext} = -\int_A \mathbf{S}_{ext} \cdot \mathbf{e}_r \mathrm{d}A. \tag{2.5}$$

2.1. SCATTERING AND ABSORPTION CROSS SECTION

The indices i, s and ext indicate the incident light, scattered light and the part of the light removed from the original beam by extinction, respectively. For the non-absorbing medium, the $W_i = 0$ and we get the relationship mentioned in the first paragraph:

$$W_{ext} = W_a + W_s. \tag{2.6}$$

The relation (2.6) only describes the overall energy. In order to get the precise values of the individual quantities W_{ext}, W_a and W_s, we have to find the amplitude scattering matrix. To do that, we need to introduce a coordinate system for the scattering plane and express the incoming light in its terms. The elements of the scattering matrix characterize the effect that every site of the particle has on the impinging light. Provided that we know the amplitude and polarization of the incoming light, we can obtain the final state of the light after its scattering grom the surface of the element of the particle element. This procedure is generally difficult, but unnecessary for further interpretation. A description of the so called Mueller scattering matrices is given in details for example in [12, p. 53] or [14].

The above mentioned procedure yields for the extinction

$$W_{ext} = I_i \frac{4\pi}{k^2} \mathrm{Re} \left(\mathbf{X} \cdot \mathbf{e}_x \right)_{\theta=0}, \tag{2.7}$$

where, for simplicity, we are considering only one scattering direction, denoted here by its unit vector $\mathbf{e}_x$. I_i stands for the intensity of the incident light and $\mathbf{X}$ is the vector scattering amplitude which is defined by the scalar scattering amplitude

$$\mathbf{X} = (S_2 \cos \phi + S_3 \sin \phi) \hat{\mathbf{e}}_{\parallel} + (S_4 \cos \phi + S_1 \sin \phi) \hat{\mathbf{e}}_{\perp}, \tag{2.8}$$

where the coefficients S_1 to S_4 are the elements of the Muller matrix expressing the amplitude of scattered light and $\hat{\mathbf{e}}_{\parallel}$ and $\hat{\mathbf{e}}_{\perp}$ are the unit vectors of the scattering plane. Dividing equation (2.7) by the incident power I_i, we get the quantity having the dimensions of area and correspondingly called the scattering cross section.

$$C_{ext} = \frac{W_{ext}}{I_i} = \frac{4\pi}{k^2} \mathrm{Re} \left(\mathbf{X} \cdot \mathbf{e}_x \right)_{\theta=0}. \tag{2.9}$$

In analogy with equation (2.6), we can write

$$C_{ext} = C_a + C_s, \tag{2.10}$$

where for C_s, we can derive the expression

$$C_s = \int_0^{2\pi} \int_0^{\pi} \frac{]\mathbf{X}]^2}{k^2} \sin \theta \, \mathrm{d}\theta \, \mathrm{d}\phi = \int_{4\pi} \frac{]\mathbf{X}]^2}{k^2} \, \mathrm{d}\Omega. \tag{2.11}$$

The fraction $|\mathbf{X}|^2/k^2$ is the differential scattering cross section and indicates the fraction of light scattered into the solid angle $(\Omega, \Omega + \mathrm{d}\Omega)$. Finally, by dividing the extinction cross section by the area, we get a dimensionless quantity called the extinction factor

$$Q_{ext} = \frac{C_{ext}}{M}, \tag{2.12}$$

where M is the projection of the particle geometrical cross-section into the plane perpendicular to the incident wave. For a sphere of the radius a the projection area is $M = \pi a^2$.

It can be seen that the size and geometry of the particles play an important role in the scattering of light, but without being a limiting factor, as might have seem. The extinction cross section can be larger than the geometrical cross-section of the particle, and consequently, the extinction coefficient may therefore be greater than unity. It is one of the examples why the extinction is such an important phenomenon in some metals. For example, gold nanospheres interact with light in an area that can be ten times larger than their actual geometric cross-section [15]. Their ability to absorb light is the reason why the well-known red color of colloidal gold solutions is very sensitive to the concentration. With increasing concentration, we soon observe that the solution becomes darker and in the end nontransparent for the light.

In the next Section, we will discuss the problem of interaction of light with a spherical object in terms of electrodynamics to find the solution for the simplest case – the quasi-static approximation. Then we will discuss some findings resulting from the Mie solution and give some outlines of the steps leading to it.

2.2. Sphere in time-dependent electromagnetic field

The starting point of our investigation will be the macroscopic Maxwell equations,

$$\nabla \cdot \mathbf{D} = \rho_{\mathbf{F}}, \tag{2.13}$$

$$\nabla \times \mathbf{E} + \frac{\partial \mathbf{B}}{\partial \mathbf{t}} = \mathbf{0}, \tag{2.14}$$

$$\nabla \cdot \mathbf{B} = \mathbf{0}, \tag{2.15}$$

$$\nabla \times \mathbf{H} = \mathbf{J_F} + \frac{\partial \mathbf{D}}{\partial \mathbf{t}}. \tag{2.16}$$

$\mathbf{E}$ is the intensity of electric field, $\mathbf{B}$ is the magnetic induction. The quantities ρ_F and $\mathbf{J_F}$ express the density of free charges and free currents density, respectively. The magnetic field $\mathbf{H}$ and dielectric displacement $\mathbf{D}$ express the response of the material to an external field:

$$\mathbf{H} = \frac{\mathbf{B}}{\mu_{\mathbf{0}}} - \mathbf{M}, \tag{2.17}$$

$$\mathbf{D} = \epsilon_{\mathbf{0}}\mathbf{E} + \mathbf{P}, \tag{2.18}$$

where μ_0 is the permeability of free space and $\mathbf{M}$ is the vector of magnetization, which is the average magnetic dipole moment per the unit volume. Electric induction is defined by the electric field from free charges and polarization $\mathbf{P}$ due to bound charges. Electric polarization is the average electric dipole moment per the unit volume and ϵ_0 is the permittivity of vacuum. Equations (2.13) – (2.16) further satisfy the following constitutive relations

$$\mathbf{J_F} = \sigma\mathbf{E}, \qquad \mathbf{B} = \mu\mathbf{H}, \qquad \mathbf{P} = \epsilon_{\mathbf{0}}\chi\mathbf{E}, \tag{2.19}$$

where conductivity σ, permeability μ and dielectric susceptibility $\chi = \epsilon_r - 1$ are empirical coefficients, characteristic for the particular material. ϵ_r is the relative permittivity of the material, defined as:

$$\epsilon_r = \frac{\epsilon(\omega)}{\epsilon_0}, \tag{2.20}$$

where $\epsilon(\omega)$ is the complex absolute permittivity of the given material. In the following text, we will only deal with non-magnetic materials, which are linear, isotropic and homogeneous. The empirical coefficients of such an idealized substance do not depend on the intensity of the external field, direction of propagation of the electromagnetic wave and, finally, on the position in the material. The relative permittivity of the material is more accurately called the dielectric function. Dielectric function has a major impact on the interaction of the substance with an external electric field. Its properties are discussed in Section 3.2 and, in more detail, in [16]. The incoming field has the form of a harmonic plane wave and can be written as

$$\mathbf{E} = E_0 \exp\left(i\mathbf{k} \cdot \mathbf{x} - i\omega t\right) \quad \textit{and} \quad \mathbf{H} = H_0 \exp\left(i\mathbf{k} \cdot \mathbf{x} - i\omega t\right) \tag{2.21}$$

where ω is the angular frequency and $\mathbf{k}$ is the complex wave vector which in isotropic and homogeneous media points in the direction of propagation

$$k = k' + ik'' \tag{2.22}$$

Physically acceptable solutions of Maxwell's equations must satisfy the Helmholtz equation. Thus, the following condition must hold for the electric field:

$$\nabla^2 \mathbf{E} + k^2 \mathbf{E} = 0. \tag{2.23}$$

2.3. Quasistatic approximation

The easiest case for the analysis of the problem is when the particle is much smaller than the wavelength of incident light. Such a situation is depicted in the Figure 2.4 The condition of validity is

$$ka \ll 1, \tag{2.24}$$

where a is the diameter of the particle. Within this approximation, the field across the volume is the same. Hence, our problem reduces to electrostatic one. We have to find the potential in the vicinity of the conductive sphere where the external field is constant but time dependent.
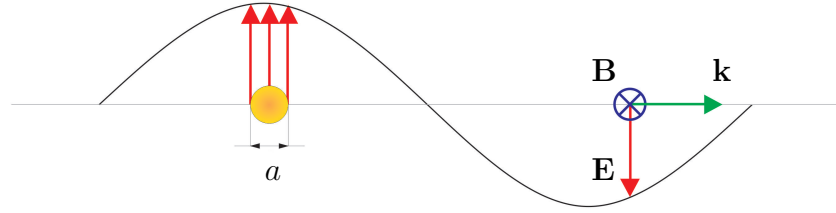

Figure 2.4: Quasistatic approximation. At any point inside the particle, the intensity of the electric field is approximately the same.

To find the distribution of the electric field near the particle, we must find a solution of the Laplace equation in spherical coordinates:

$$\nabla^2 \varphi = 0, \tag{2.25}$$

where φ is the electrostatic potential, the negative gradient of which is the electric field. The boundary conditions require i) continuity of potential at the sphere surface, ii) continuity of the normal component of the vector $\mathbf{D}$. The solution takes the form of spherical harmonic functions, which are defined by the Legendre polynomials, and functions of the type $e^{im\phi}$, see Figure 2.5. Step by step derivation can be found in [17, p. 26]. For further explanation, it is important that the radial part of the solution has the form r^l and $r^{-(l+1)}$, where $l = (0, 1, 2, \dots)$. The general solution of the Laplace equation can be written in the form

2.3. QUASISTATIC APPROXIMATION

$$\varphi(r, \vartheta) = \sum_{l=0}^{\infty} (A_l r^l + B_l r^{-l-1}) P_l(\cos \theta). \tag{2.26}$$

If we choose $l = 1$, we get for the potential

$$\varphi_i = Ar \sin(\theta) \cos(\varphi) \qquad \text{inside the sphere,} \tag{2.27}$$

$$\varphi_e = \left(E_0 r + \frac{B}{r^2} \right) \sin(\theta) \cos(\varphi) \qquad \text{outside the sphere.} \tag{2.28}$$

The constants are complex and can be determined by applying the boundary conditions. By differentiation of the potential, we get the electric field in the proximity of the sphere:

$$\mathbf{E}_e = \mathbf{E}_0 r - a^3 \alpha \mathbf{E}_0 \left(\frac{R^3}{r^3} e_r - \frac{3R^3}{r^3} e_\psi \right), \tag{2.29}$$

where α is the dipolar polarizability and has the form

$$\alpha = \frac{\epsilon_i - \epsilon_o}{\epsilon_i - 2\epsilon_o}. \tag{2.30}$$

ϵ_i a ϵ_o are the dielectric functions inside and outside the object, respectively. The polarizability is also a complex function and its value reflects the "willingness" of a material to the dipolar charge distribution in response to the excitation field.

This quantity is closely linked to plasmon resonances in the material. The phenomenon known as localized surface plasmon (LSP) arises when the polarizability reaches its maximum. It is described mathematically by the so called Fröhlich condition which can be found as an extreme value of polarizability. As can be seen from (2.30), this state occurs when:

$$\epsilon_i = 2\epsilon_o. \tag{2.31}$$

We have introduced the scattering coefficient by equation (2.12). For our quasi-static case the scattering coefficient is

$$Q_{scat} = \frac{8}{3} x^4 \text{ Im} \left| \frac{\epsilon_i - \epsilon_o}{\epsilon_i - 2\epsilon_o} \right|^2 \tag{2.32}$$

and the absorption coefficient is

$$Q_{abs} = 4x \text{ Im} \frac{\epsilon_i - \epsilon_o}{\epsilon_i - 2\epsilon_o}, \tag{2.33}$$

where $x = 2\pi a/\lambda$. If we choose $l = 2$ in equation (2.26), the expression for the field close to the particle surface will contain higher orders of the expansion. Higher orders carry the term β, representing the quadrupolar polarizability:

$$\beta = \frac{\epsilon_i - \epsilon_o}{\epsilon_i + 3/2\epsilon_o}. \tag{2.34}$$

Quadrupolar polarizability cannot be omitted for larger particles. In the denominator of equation (2.34), we have the factor 3/2. In equation for the dipolar mode (2.30), there

$$l = 0, m = 0 \qquad l = 1, m = 0 \qquad l = 1, m = 1 \qquad l = 2, m = 0$$
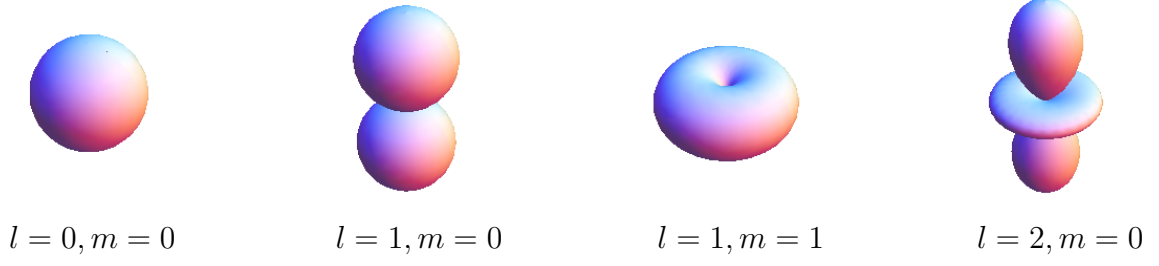
Figure 2.5: Spherical harmonic functions. The first four spherical functions are depicted to illustrate the solution of laplace equation in spherical coordinates.

is the factor 2. These coefficients arise from the spherical radial terms of the Laplace equation r^l and $r^{-(l+1)}$. For the dipole polarization we have $l = 1$ and the ratio of the magnitudes of the exponents is $(l + 1)/l = 2$. For quadrupole excitation, $l = 2$ and $(l + 1)/l = 3/2$. The absorption and scattering coefficients given by the dipolar and quadrupolar contribution are then:

$$Q_{abs} = 4x\mathrm{Im}\left[\alpha + \frac{x^2}{12}\beta + \frac{x^2}{30}(\epsilon_i - 1)\right], \tag{2.35}$$

$$Q_{scat} = \frac{8}{3}x^4\left[|\alpha|^2 + \frac{x^4}{240}|\beta|^2 + \frac{x^4}{900}|\epsilon_i - 1|^2\right]. \tag{2.36}$$

An example of the absorption spectrum is shown in Figure 2.6. We can modify the equations for the polarizabilities to yield directly the resonant frequency of the desired mode

$$\epsilon_i = -\epsilon_o\frac{l + 1}{l} \qquad l = 1, 2, 3... \tag{2.37}$$
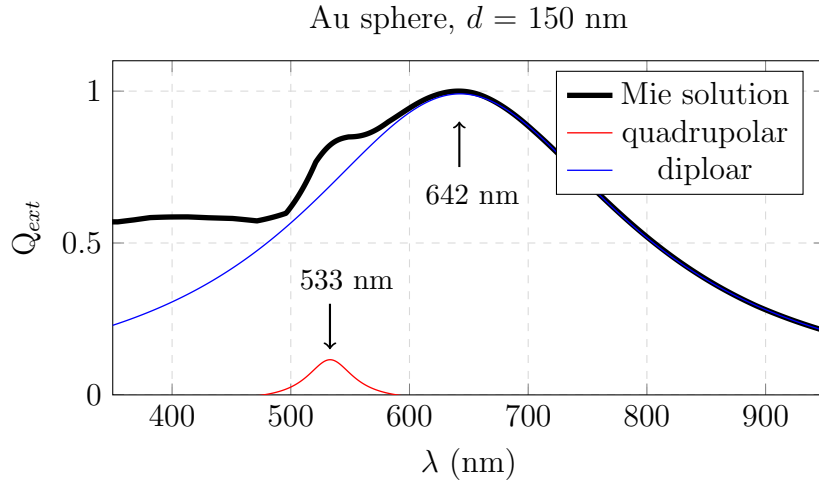

Figure 2.6: Extinction spectrum of the gold sphere with the diameter 150 nm. The surrounding medium has the refractive index $n = 1.33$. The maximum at the wavelength 642 nm is the dipolar excitation. The quadrupolar excitation is located at the wavelength 533 nm. The data fitted by Lorentz functions.

2.4. Sphere of an arbitrary size

In this section, an outline is given to the procedure that leads to the solution of the interaction of electromagnetic radiation with spherical particles without the limits imposed on their size. Thus we will leave the condition expressed by equation (2.24) and will deal with particles of a generally arbitrary radius. Probably, the most famous works published on this topic is an article by Gustav Mie from 1908 [9]. Mie applied an analytical approach to explain the color of suspensions containing metallic particles. He assumed that the particles have a spherical shape and are infinitely dispersed in a solution.

Soution of Maxwell's equations for spherical particles with dimensions comparable to the wavelength of light appeared in scientific articles even before 1900 as documented by Lilienfeld [18]. Mie was not the first one interested in this topic, however the previous works did not come to a wider awareness.

Mie's work also did not achieve a special attention after its publication. Neither the author himself considered it seminal. Its main advantage compared to the preceding works is that its main part is devoted to the interpretation of experimental results based on the presented theory. Mie gives a number of examples that provide, at least until then, hardly accessible insight into the effects of the diffusion environment. The compact and clarifying explanation together with the methodology which expresses the solution in a form suitable for numerical calculations are Mie's main contributions. This solution has the form of infinite series.

In the early 20th century the calculations had to be done by hand and the computations were thus practically limited to the sum of the first three terms of the series. Even with this restriction, Mie could predict the properties of particles with sizes roughly up to 200 nm in diameter [18] for the wavelengths in the visible range of the spectrum. With the development of computers, numerical methods have become a convenient tool for obtaining relatively quick solutions valid for larger particles in a wide range of wavelengths. The programs that implement algorithms for Mie series are often used in astronomy or meteorology today. Although the solution is accurate, real particles are often not perfectly spherical. Mie was aware of this fact and pointed out that a similar approach should be found for ellipsoidal particle shapes. However, in many cases the particles can be considered as spherical and we can still get accurate results.

2.4.1. The Mie solution

Mie's analytical approach to the spherical problem employs particular vector harmonic functions constructed to fulfill requirements imposed on electromagnetic fields and to respect the symmetry of the problem. The complete derivation is shown in [9], here we will only mention the most important steps of those presented in [12].

Let us look for a vector function $\mathbf{M}$ consisting of the scalar function ψ and certain constant vector $\mathbf{c}$

$$\mathbf{M} = \nabla \times (\mathbf{c}\psi). \tag{2.38}$$

Such vector function will satisfy the vector wave equation for each ψ that is a solution of the scalar wave equation

$$\nabla^2 \, \mathbf{M} + k^2 \, \mathbf{M} = \nabla \times [\mathbf{c} \, (\nabla^2 \psi + k^2 \psi)], \tag{2.39}$$

and $\mathbf{M}$ satisfies the Helmholtz equation (2.23). With the vector function $\mathbf{M}$, we can construct a function $\mathbf{N}$ given by the relation

$$\mathbf{N} = \frac{\nabla \times \mathbf{M}}{k}. \tag{2.40}$$

$\mathbf{N}$ as well as $\mathbf{M}$ have the zero divergence and are the solutions of the vector wave equation. Thus both functions have the properties of electromagnetic field vectors and are bound to each other by the relations of rotations. With this definition of the functions $\mathbf{M}$ and $\mathbf{N}$, the problem to describe the field, is reduced to a more simple problem of finding solution to the scalar wave equation for the function ψ.

$$\nabla^2 \psi + k^2 \psi = 0. \tag{2.41}$$

The function ψ is the *generating* function which creates a vector harmonic functions $\mathbf{M}$ and $\mathbf{N}$, and the vector $\mathbf{c}$ is called the guiding vector.

We express the equation (2.41) in the spherical coordinates

$$\frac{1}{r^2}\frac{\partial}{\partial r}\left(r^2\frac{\partial \psi}{\partial r}\right) + \frac{1}{r^2 \sin\theta}\frac{\partial}{\partial \theta}\left(\sin\theta\frac{\partial \psi}{\partial \theta}\right) + \frac{1}{r^2 \sin\theta}\frac{\partial^2 \psi}{\partial^2 \Phi} + k^2\psi = 0. \tag{2.42}$$

The particular solution can be sought in the form of the product of three independent functions on single variables

$$\psi(r, \theta, \phi) = R(r)\Theta(\theta)\Phi(\phi), \tag{2.43}$$

which gives us three independent equations, each for one coordinate:

$$\frac{\mathrm{d}^2\Phi}{\mathrm{d}\phi^2} + m^2\Phi = 0, \tag{2.44}$$

$$\frac{1}{\sin\theta}\frac{d}{d\theta}\left(\sin\theta\frac{\mathrm{d}\Theta}{\mathrm{d}\theta}\right) + \left[n(n+1) - \frac{m^2}{\sin^2\theta}\right]\Theta = 0, \tag{2.45}$$

$$\frac{\mathrm{d}}{\mathrm{d}r}\left(r^2\frac{\mathrm{d}R}{\mathrm{d}r}\right) + [k^2r^2 - n(n+1)]R = 0, \tag{2.46}$$

where the constants m and n can be determined by the auxiliary conditions imposed on the function ψ. The solution for equation (2.44) are the harmonic functions

$$\Phi_1 = \cos m\phi, \qquad \Phi_2 = \sin m\phi, \tag{2.47}$$

where $m = (0, 1, 2, \dots)$. The solution that satisfies equation (2.45) is the eigenfunction of the ∇ operator in spherical coordinates. These functions are the *Legendre functions* of the first kind:

$$P_n^m(\cos\theta), \qquad n = m, m+1, \dots$$

where n is the degree and m is the order of the function. When $m = 0$, we have the *Legendre polynomials* with the degree n. The last equation (2.46) is satisfied by the *Bessel functions* of the first and second kind denoted as J_ν and N_ν, respectively. The linearly independent solutions of the equation (2.46) are:

$$j_\nu(\rho) = \sqrt{\frac{\pi}{2\rho}}J_\nu(\rho), \tag{2.48}$$

$$n_\nu(\rho) = \sqrt{\frac{\pi}{2\rho}} N_\nu(\rho), \qquad (2.49)$$

where $\rho = kr$ is a dimensionless variable and $\nu = n + 1/2$. Any linear combination of the solutions in the form of equations (2.48) and (2.49) represents again a solution. In particular, the complex *spherical Bessel functions of the third kind*, referred to as *Hankel functions*, are defined by these functions as:

$$h_n^{(1)}(p) = j_n(\rho) + iy_n(\rho), \qquad (2.50)$$

$$h_n^{(2)}(p) = j_n(\rho) - iy_n(\rho). \qquad (2.51)$$

We can now construct the generating function that is a solution of the scalar wave equation (2.41)

$$\psi_{1mn} = \cos m\phi \ P_n^m(\cos\theta)z_n(kr), \qquad (2.52)$$

$$\psi_{2mn} = \sin m\phi \ P_n^m(\cos\theta)z_n(kr), \qquad (2.53)$$

where z_n can be any of the spherical Bessel functions j_ν, n_ν, $h_n^{(1)}$ or $h_n^{(2)}$. With the knowledge of the scalar wave equation solution, we can generate the vector spherical harmonics as:

$$\mathbf{M}_{1mn} = \nabla \times (\mathbf{r}\psi_{1mn}), \qquad \mathbf{M}_{2mn} = \nabla \times (\mathbf{r}\psi_{2mn}), \qquad (2.54)$$

$$\mathbf{N}_{1mn} = \frac{\nabla \times \mathbf{M}_1 mn}{k}, \qquad \mathbf{N}_{2mn} = \frac{\nabla \times \mathbf{M}_2 mn}{k}. \qquad (2.55)$$

The objective now is to express a plane x-polarized wave as an expansion written in terms of the vector harmonic functions. The plane wave in spherical coordinates is

$$\mathbf{E}_i = E_0 \mathrm{e}^{ikr\cos\phi}\hat{\mathbf{e}}_x. \qquad (2.56)$$

The sought expansion is

$$\mathbf{E}_i = \sum_{m=0}^{\infty}\sum_{n=0}^{\infty} B_{1mn}\mathbf{M}_{1mn} + B_{2mn}\mathbf{M}_{2mn} + A_{1mn}\mathbf{N}_{1mn} + A_{2mn}\mathbf{N}_{2mn}), \qquad (2.57)$$

where A_{1mn}, A_{2mn}, B_{1mn} and B_{2mn} are constants to be determined. We are not presenting the individual steps leading to their finding here, but we just note that relation of orthogonality between the vector harmonic functions is of the frequent use here. By some manipulation we obtain

$$B_{1mn} = \frac{\int_0^{2\pi}\int_0^{\pi} \mathbf{E}_i \cdot \mathbf{M}_{1mn} \sin\theta \ \mathrm{d}\theta\mathrm{d}\phi}{\int_0^{2\pi}\int_0^{\pi} |\mathbf{M}_{1mn}|^2 \sin\theta \ \mathrm{d}\theta\mathrm{d}\phi}. \qquad (2.58)$$

Similar definition stands for B_{2mn}, A_{1mn} and A_{2mn}. Again by applying orthogonality we find that $B_{2mn} = A_{1mn} = 0$ for all m and n except for $m = 1$. Further requirement to be met is the finite value of the field at the origin. This implies that the only acceptable Bessel function is $j_\nu(kr)$ as the Bessel functions of the second kind diverge at the origin. To denote this, we use the subscript j for the constants. Then, the expansion is

$$\mathbf{E}_i = \sum_{n=1}^{\infty} \left(B_{1jn}\mathbf{M}_{1jn}^{(1)} + A_{2jn}\mathbf{N}_{2jn}^{(1)} \right). \qquad (2.59)$$

The coefficients B_{1jn}, A_{2jn} can be evaluated using the formula (2.58). So we get the expansion coefficients

$$B_{1jn} = i^n E_0 \frac{2n+1}{n(n+1)} \tag{2.60}$$

and

$$A_{2jn} = -iE_0 i^n \frac{2n+1}{n(n+1)}. \tag{2.61}$$

Hence we arrive to the final expression of the expansion of a plane electromagnetic wave in spherical vector harmonic functions:

$$\mathbf{E}_i = E_0 \sum_{n=1}^{\infty} i^n \frac{2n+1}{n(n+1)} \left(\mathbf{M}_{1jn}^{(1)} - i\mathbf{N}_{2jn}^{(1)} \right). \tag{2.62}$$

This expression can be inserted into the Maxwell equations and we can analyze the problem to find the desired quantities. For us, the external scattered field is of the main interest. In the surroundings of the particle, we are far from the origin and we can use the Bessel functions of the first and second type. The compact way to write the solution is to employ the Hankel functions. In asymptotic limit, where $kr > n^2$, we can write for them:

$$h_n^{(1)}(kr) \sim \frac{(-i)^n e^{ikr}}{ikr}, \tag{2.63}$$

$$h_n^{(2)}(kr) \sim -\frac{i^n e^{-ikr}}{ikr}. \tag{2.64}$$

The function $h_n^{(1)}(kr)$ corresponds to the diverging (outgoing) spherical wave and the function $h_n^{(2)}(kr)$ represents the convergent (incoming) spherical wave. So if we are interested strictly in the scattered light further from the surface of the particle, we should take into account only $h_n^{(1)}(kr)$. Finally, the expansions for the scattered field are:

$$\mathbf{E}_s = \sum_{n=1}^{\infty} E_n (ia_n \mathbf{N}_{2jn}^{(3)} - b_n \mathbf{M}_{1jn}^{(3)}), \tag{2.65}$$

$$\mathbf{H}_s = \frac{k}{\omega\mu} \sum_{n=1}^{\infty} E_n (ib_n \mathbf{N}_{1jn}^{(3)} - b_n \mathbf{M}_{2jn}^{(3)}), \tag{2.66}$$

here the superscript (3) denotes the vector harmonics with the radial component given by the Bessel functions of the third kind $h_n^{(1)}$.

We have found the scattered field in the form of spherical harmonics functions. Or, in another words, in the form of electromagnetic normal modes of a conductive sphere.

$$\mathbf{M}_{1jn} = \cos\phi \, \pi_n(\cos\theta) z_n(\rho)\hat{\mathbf{e}}_\theta - \sin\phi \, \tau_n(\cos\theta) z_n(\rho)\hat{\mathbf{e}}_\phi, \tag{2.67}$$

$$\mathbf{M}_{2jn} = -\sin\phi \, \pi_n(\cos\theta) z_n(\rho)\hat{\mathbf{e}}_\theta - \cos\phi \, \tau_n(\cos\theta) z_n(\rho)\hat{\mathbf{e}}_\phi, \tag{2.68}$$

$$\mathbf{N}_{1jn} = \sin\phi \, n(n+1)\sin\theta \, \pi_n(\cos\theta)\frac{z_n(\rho)}{\rho}\hat{\mathbf{e}}_r \; + \; \sin\phi \, \tau_n(\cos\theta)\frac{[\rho z_n(\rho)]'}{\rho}\hat{\mathbf{e}}_\theta$$
$$+ \; \cos\phi \, \pi_n(\cos\theta)\frac{[\rho z_n(\rho)]'}{\rho}\hat{\mathbf{e}}_\phi, \tag{2.69}$$

$$\mathbf{N}_{2jn} = \cos\phi\; n(n+1)\sin\theta\; \pi_n(\cos\theta)\frac{z_n(\rho)}{\rho}\hat{\mathbf{e}}_r \;+\; \cos\phi\; \tau_n(\sin\theta)\frac{[\rho z_n(\rho)]'}{\rho}\hat{\mathbf{e}}_\theta$$
$$-\;\sin\phi\; \pi_n(\cos\theta)\frac{[\rho z_n(\rho)]'}{\rho}\hat{\mathbf{e}}_\phi. \tag{2.70}$$

In the equations (2.67) – (2.70), we introduced the functions π_n and τ_n. These are called the *angle-dependent functions* defined as

$$\pi_n = \frac{P_n^1}{\sin\theta}, \qquad \tau_n = \frac{\mathrm{d}P_n^1}{\mathrm{d}\theta}. \tag{2.71}$$

The polar plots of these functions are depicted in Figure 2.7. The diagrams show that for every n there is always the forward loop but the backward one sometimes disappears. The vector harmonics are superpositions of the π_n and τ_n functions and the bigger the particle the higher orders of angular-dependent functions are included in the $\mathbf{N}$ and $\mathbf{M}$ functions. As a consequence, the forward scattering is predominant over backscattered and the forward loop is getting narrower.
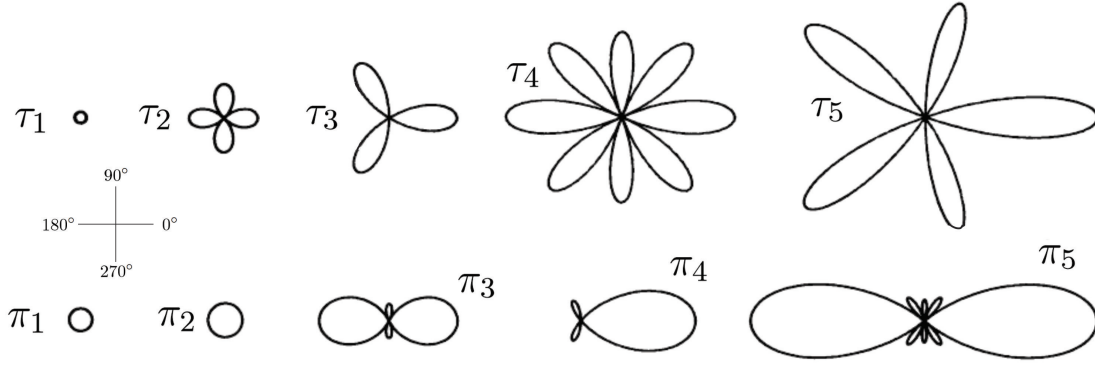

Figure 2.7: Polar plots of angle dependent functions π_n and τ_n. The field with respect to θ. The image reproduced from [12].

Figure 2.8 shows the electric field lines for the first four modes of charge distribution inside the sphere. For each n, there are two modes. The a_1 – a_4 are the TM modes and b_1 – b_4 show the TE modes. Without going into details, for every mode denoted by the letter n, there are four coefficients a_n, b_n, c_n and d_n. The coefficients a_n and b_n describe the scattered field (see eqs. (2.65) and (2.66)) and c_n and d_n are for the internal field. We present just the scattering coefficients written for convenience using the *Ricatti-Bessel functions* defined as

$$\psi_n(\rho) = \rho j_n(\rho), \qquad \xi_n(\rho) = \rho h_n^{(1)}(\rho). \tag{2.72}$$

The coefficients are:

$$a_n = \frac{m\psi_n(mx)\psi_n'(x) - \psi_n(x)\psi_n'(mx)}{m\psi_n(mx)\xi_n'(x) - \xi_n(x)\psi_n'(mx)}, \tag{2.73}$$

$$b_n = \frac{\psi_n(mx)\psi_n'(x) - m\psi_n(x)\psi_n'(mx)}{\psi_n(mx)\xi_n'(x) - m\xi_n(x)\psi_n'(mx)}, \tag{2.74}$$

where m is the relative refractive index $m = k_1/k = N_1/N$, where k_1 and k are the wave vectors of light (and N_1 and N are the refractive indexes) in the sphere and in the ambient

medium respectively. We should point out that for m approaching unity the coefficients tend to vanish, condition that obviously has to be satisfied. The coefficients for internal and scattered fields are strongly related as the denominator of a_n and d_n, and of b_n and c_n are the same. We have mentioned above that the expansion for the scattered field is the sum containing a particular number of modes. If for the certain mode, i.e. specific n in the expression, the denominator is very small or approaches zero, this mode will become dominant in the scattering spectra. The modes for which the condition of minimum of the denominators is exactly fulfilled are called *the natural modes of the sphere.* In the general case, the resulting mode is the superposition of normal modes. We shall be interested mostly in the surface modes that are discussed in Chapter 3.
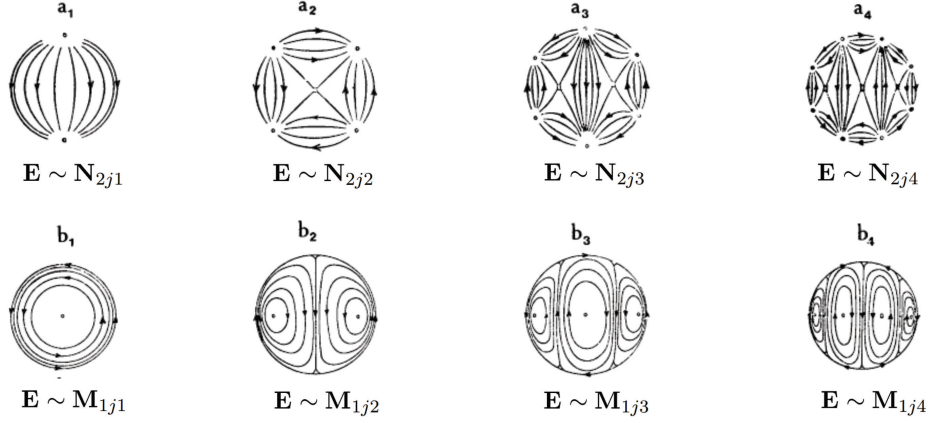

Figure 2.8: Electric field inside the particle. Image reproduced from [12].

In section 2.1 we have introduced the cross-sections as the convenient mean to represent optical behavior of the particle under study. We used the Poynting vector to quantify the amount of electromagnetic radiation scattered and absorbed by the particle. We used the results derived by using the concept of amplitude scattering and Mueller matrices. Here we have expansions for the scattered field and we can substitute them into the equation for the flux of the Poynting vector through the enclosed surface:

$$W_{ext} = \frac{1}{2}Re \int_0^{2\pi} \int_0^{\pi} (E_{i\phi}H*_{s\theta} - E_{i\theta}H*_{s\phi} - E_{s\theta}H*_{i\phi} + E_{s\phi}H*_{i\theta})r^2 \sin\theta \ d\theta d\phi, \quad (2.75)$$

$$W_s = \frac{1}{2}Re \int_0^{2\pi} \int_0^{\pi} (E_{s\theta}H*_{s\phi} - E_{s\theta}H*_{s\theta})r^2 \sin\theta \ d\theta d\phi, \quad (2.76)$$

In the end we can rewrite the formulas into the forms giving the particle cross-sections, each expressed in the terms of expansion coefficients. For the scattering cross-section we have

$$C_s = \frac{W_s}{I_i} = \frac{2\pi}{k^2} \sum_{n=1}^{\infty} (2n+1)\left(|a_n|^2 + |b_n|^2\right), \quad (2.77)$$

and for extinction

$$C_{ext} = \frac{W_{ext}}{I_i} = \frac{2\pi}{k^2} \sum_{n=1}^{\infty} (2n+1)Re\{a_n + b_n\}. \quad (2.78)$$

These summations are the central part of numerical programs and applications that calculate light scattering on the basis of the Mie theory.

Chapter 3

Small particles

The aim of this thesis is to analyze the optical response of noble metal particles with the sizes starting at 5 nm in diameter. It can be shown, on the basis of the Mie theory, that the emergence of higher excitation modes comes with an the increasing diameter of the particle. For the large particles, comparable to the wavelength of the incident light, multipolar excitations are present as we are beyond the quasistatic limit and the particle feels a nonhomogeneous field over its volume. This leads to the higher radiation, enhanced scattering effects and broadening of the spectrum [19]. On the contrary, simulations show that the scattered field almost does not contribute to the overall extinction for the particles up to 60 nm in diameter. For the particles below this size the absorption is a predominant phenomenon. The energy absorption occurs mainly through the decay of surface plasmon modes, i.e. through the surface damping effect on the oscillating electrons and phonon interactions. The surface scattering is caused by the spatial confinement of light. This effect is particularly strong when the size is reduced below the length corresponding to the electron mean free path. The surface modes are determined by the free charge redistribution in the response to the external field. This distribution depends on the particle morphology and its fingerprints become readable when the size is decreased to several nanometers, see Figure 3.1.

The fact that optical properties of nanoparticles are sensitive to their shape is of great importance for the possibility of tunable optical response. The NP's spectra exhibit specific features where no effects are observed for the bulk samples. These absorption peaks are mainly the function of the shape and size of the scatterer. The confinement is manifested by increased damping that affects the profile of the peak. In order to model these changes, we present in Section 3.2 the correction of the dielectric function based on the Drude model.

3.1. Shape and size effects

To each plasmon resonance with certain initial surface distribution of charge, we can assign the mode of oscillation called the *surface mode*. For the spherical particles, these modes are easy to find [12]. However, it requires more effort to uncover the modes induced in arbitrarily shaped particle, see [20].

For spherical particles, we can recall the expansions we derived in Section 2.4. The condition of maximum of the scattering coefficient for a small sphere can be written in terms of the order of the spherical Bessel function n and index of refraction m as

$$m^2 = -\frac{n+1}{n}. \qquad n = 1, 2, \ldots \tag{3.1}$$

For this condition, the scattering coefficient is infinite. The corresponding frequencies are complex, but there are close frequencies that are real and for them the scattering will be strong. The designation *surface modes* refers to the behavior of the corresponding internal field. This field is radial and with higher mode orders the field is concentrated closer and closer to the surface of the sphere. The mode with $n = 1$ is called the *mode of a uniform polarization* and fulfills the Fröhlich condition for the maximum 2.31. The similar expression follows from electrostatics equation (2.33). From the higher term of expansions derived by Mie, we can see the effect of the size on the Fröhlich frequency

$$\epsilon = -\left(2 + \frac{15}{5}x^2\right)\epsilon_m, \tag{3.2}$$

where $x = 2\pi a/\lambda$. For an increasing size parameter x, the frequency is shifted to the longer wavelengths.

3.1.1. Nonspherical particles

Ellipsoidal particles can be treated in the similar way by using the elliptical coordinate system. In a quasistatic approach we need to solve Laplace's equation in ellipsoidal coordinates. We state here only the polarizability when the electric field is parallel to the i-th axis:

$$\alpha_i = 4\pi\, abc\, \frac{\epsilon_1 - \epsilon_m}{3\epsilon_m + 3L_3(\epsilon_1 - \epsilon_m)} \tag{3.3}$$

where a, b and c are the lengths of the semiaxes and L_3 is the geometrical factor. The dipole moment is then

$$\mathbf{p} = \alpha_i\mathbf{E}_0. \tag{3.4}$$

Other analytical models have been made for spheroids [21] and similar shapes. The extensive overview is given in [22].

The effect of the geometry was investigated carefully in recent years [19, 23–25]. We will present the conclusions made in [19] providing the insight into the effects of the shape variations supported by numerical simulations. The investigation was carried out for the shapes that evolve from cubic to spherical shapes through increasing truncation. The calculated spectra are shown in Figure 3.1 for 4.5 nm silver nanoparticles immersed in a medium with the refractive index n= 1.47.

We can see that the particles with fewer facets exhibit more complicated extinction efficiency patterns in the spectra. Their most intensive peaks are also red-shifted with respect to the sphere. As the particle shape gets more and more symmetric, its resonance wavelength is moving towards higher energies (blue shift) and gets more symmetric shape together with a decrease of the FWHM. In case of cuboctahedron, we can still observe
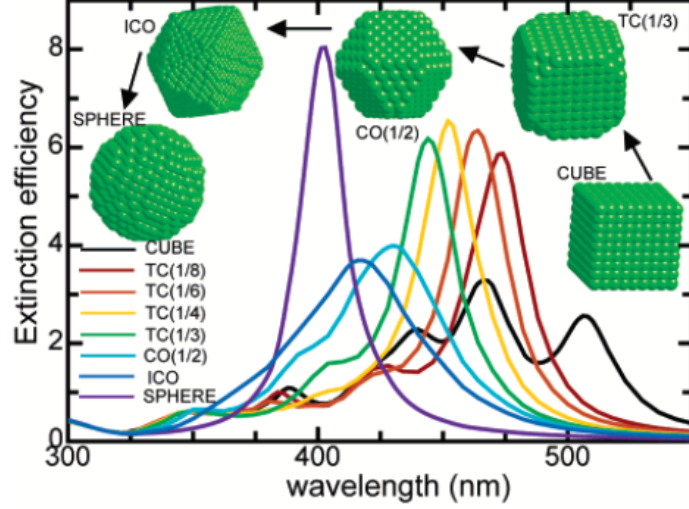
Figure 3.1: Extinction efficiency spectra of silver nanoparticles with the size 4.5nm. The simulated shapes are: cube, truncated cube with truncation at various fractions of the side-length (TC 1/8, TC 1/6, TC 1/4, TC 1/3), cuboctahedron (CO 1/2), icosahedron (ICO) and sphere. Figure taken from [19]

the individual peaks of the modes in the profile of the spectrum. Finally, the sphere, constructed of an infinite number of facets, has only one resonance frequency.

Here, the influence of the ambient medium is advantageous. The higher refractive index, the higher the mutual resonance frequency shift between the peaks within each spectrum and, moreover, the shift is generally more significant for longer wavelengths. This allows us to resolve easier the spectra because the individual modes are more separated and the spectra are easier to read.

3.1.2. Rods

Nanorods and plasmonic antennas represent a promising area for many applications, especially in sensing, energy confinement or guiding, and others. The shape evolution to elongated nanoparticles is characteristic by the emergence of the transversal (TM) and longitudinal (LM) modes induced in the particle. Noble metal nanorods are the subject of an active investigation for their optical tunability and biocompatibility. Usually, numerical techniques are employed to study optical properties of nanorods, see Lee [26] or Brioude [27], although an analytical approach has also been developed, see Kalousek et. al. [28].

The most significant property of the elongated nanoparticles is the presence of LM and TM modes, characterized by the presence of two extinction maxima in the spectra. There is a growing difference in the intensity and distance of the corresponding two resonances as the aspect ratio increases. The more intensive longitudinal resonance is also located at higher wavelengths whereas the transversal surface plasmon mode is less intense and corresponds to the smaller wavelengths. The position of the main peak (the longitudinal resonance) is a sensitive function of the particle aspect ratio, see Table 3.1. The position of longitudinal and transversal mode can be qualitatively explained if we consider the charge redistribution in the reaction to the presence of the external field, see Figure 3.2. In the
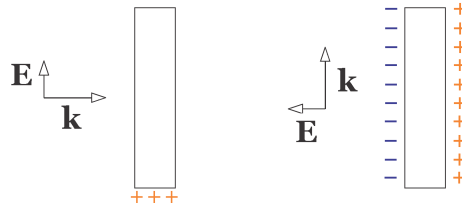
Figure 3.2: Surface charge distribution of the nanorod in the presence of linearly polarized field. Situation on the left corresponds to the light polarized parallel to the main axis of nanorod, inducing longitudinal plasmon resonance. Perpendicular polarization on the right, inducing polarization of the surface that gives rise to the transversal plasmon resonance. Image taken from [15].

case, when the light is polarized perpendicularly to the main axis of the rod, the field created inside the rod is stronger than in case of the parallel polarization. Stronger field results in bigger driving force acting on the free electrons. In analogy with the driven oscillatory motion, we can expect higher frequency of oscillation which means shorter wavelength.

Link, Mohamed and El-Sayed [29] found this shift to be linear in vacuum and nonlinear in the medium with the refractive index higher than one. They assign this nonlinearity to the effect of the capping layer. Its presence on the nanorod surface changes the effective index of refraction.

Diameter (nm)	Length (nm)	Aspect ratio	Plasmon resonance (nm)
10	102	10.2	1400
10	81	8.1	1200
10	67	6.7	1064
10	59	5.9	980
10	50	5	900
10	45	4.5	850
10	41	4.1	808
10	38	3.8	780
10	35	3.5	750
10	29	2.9	700

Table 3.1: Longitudinal surface plasmon resonances of gold nanorods as a function of the aspect ratio of the nanorod. Table taken from *http://www.nanopartz.com*.

3.2. Dielectric function

The behavior of the material in electric field is described by its dielectric function. If the material is homogeneous and isotropic, the dielectric function is only a function of the frequency of the external field, regardless of the position in the sample or the direction of propagation:

$$\epsilon(\omega) = \epsilon' + i \, \epsilon''. \tag{3.5}$$

From the constitutive relations (2.19) we know that permittivity is connected with susceptibility. These quantities express how the material reacts on the presence of electric

field. Permittivity describes directly the ability to create electric field by the particles in the material whereas susceptibility is often related to the ease of polarization. Drude proposed a model of free electrons suitable for the description of conduction electrons in metals. In his model, ionic cores form fixed lattice points and electrons move freely in their matrix. Damping is caused by collisions of electrons with the lattice atoms. The equation of motion for a single electron is

$$m_e \frac{\mathrm{d}^2 \mathbf{x}}{\mathrm{d}t^2} = q\mathbf{E} - m_e \frac{1}{\tau} \frac{\mathrm{d}\mathbf{x}}{\mathrm{d}t}, \tag{3.6}$$

where τ is the relaxation time, i.e. in principle the average time between two collisions of the electron with lattice atoms. Later, when we will be considering additional damping, we will switch to the damping constant

$$\gamma_0 = \frac{1}{\tau}, \tag{3.7}$$

which has the units of frequency s^{-1}. The solution of equation (3.6) is

$$\mathbf{x}(t) = \frac{q}{m_e(\omega^2 + i\omega/\tau)} \mathbf{E}(t). \tag{3.8}$$

The polarization is given by the relation $\mathbf{P} = ne\mathbf{x}$. By comparison with the constitutive relation for polarization (2.19) and introducing the plasma frequency $\omega_p^2 = ne^2/(\varepsilon_0 m_e)$, we get for the dielectric function:

$$\epsilon(\omega) = 1 - \frac{\omega_p^2}{\omega^2 + i\omega/\tau}. \tag{3.9}$$

This is the permittivity of the free electron gas as derived by Drude, see Figure 3.3. We can apply this result to conduction electrons in metals being considered to move freely in the material.

The disagreement found between the Mie solution and the experiment for small particles suggests to revise the dielectric function. One of the tempting explanation could be to assign the difference to the dominance of a quantum behavior of electrons when these are confined in a small volume. Then our dielectric function may become inapplicable for it was measured for the bulk material. Recently, the properties of silver spherical dimers were studied [25]. Their optical properties were calculated using a quantum mechanical model of free electrons and the simulation agrees with the experimental data. The quantum mechanical model was found suitable for sizes bellow approximately 6 nm. In this region, the bulk properties of the band structure are lost and dielectric function exhibits absorption effects that resemble the transitions present in single atoms.

In our calculations, we used the so called Free Path Effect model (FPE) proposed by Kreibig in [31]. Using this model, we can find the expression for the size dependent damping constant. In this model, the surface of the particle is considered a scatterer for the conduction electrons. There are many models used to derive expression for the effective mean free path, see for example [23, 32, 33]. We present here the derivation published by Kreibig [31].

The effective mean free path of the conduction electron is

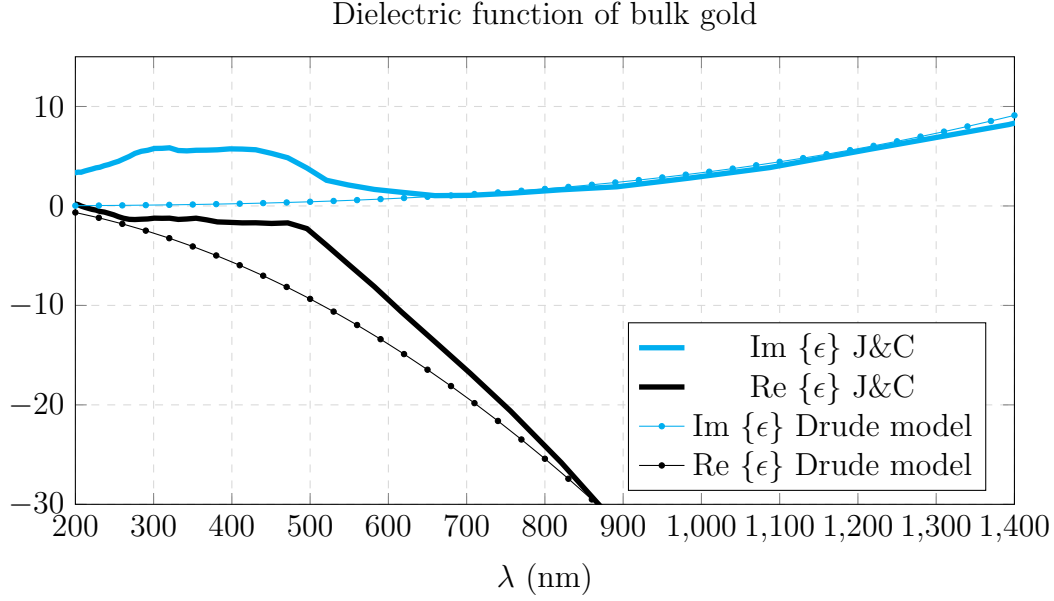$$L_{eff} = \frac{\int L(\theta)\mathrm{d}w}{\int \mathrm{d}w}, \tag{3.10}$$

Figure 3.3: Dielectric function of bulk gold. Interpolated data measured by Johnson and Christy [30] (solid line) are compared with the Drude model (dots).

where $L(\theta)$ is the free path of an electron leaving an infinitesimal surface area $\mathrm{d}f$ at an angle θ with respect to its normal and $\mathrm{d}w$ is the number of scattering events per unit time. The scattering angle distribution is assumed to be defined by the Lambert cosine law

$$\mathrm{d}w = A \cdot \mathrm{d}f \cos\theta \mathrm{d}\Omega, \tag{3.11}$$

where Ω is the solid angle and A is the constant. For example, for the sphere of the radius R, we get a simple expression

$$L_{sphere} = \frac{4}{3}R. \tag{3.12}$$

Different models give different multiplication constants. However, generally all the derivations yield the surface damping term γ_A to be of the form

$$\gamma_A = B\frac{v_F}{L_{eff}}, \tag{3.13}$$

where the constant B varies for the particular shape and physical model and v_F is the Fermi velocity. The overall collision frequency is

$$\gamma_{net}(L_{eff}) = \gamma_0 + \gamma_A = \gamma_0 + B\frac{v_F}{L_{eff}}, \tag{3.14}$$

where γ_0 is the damping due to interactions of conduction electrons with phonons, i.e. lattice atoms, or impurities in the material, and γ_A represents the collisions with the surface of the particle.

To find the dielectric function of the particle smaller than the mean free path of the conduction electron, we assume that the experimentally measured dielectric function is the sum of interband and intraband electron transitions:

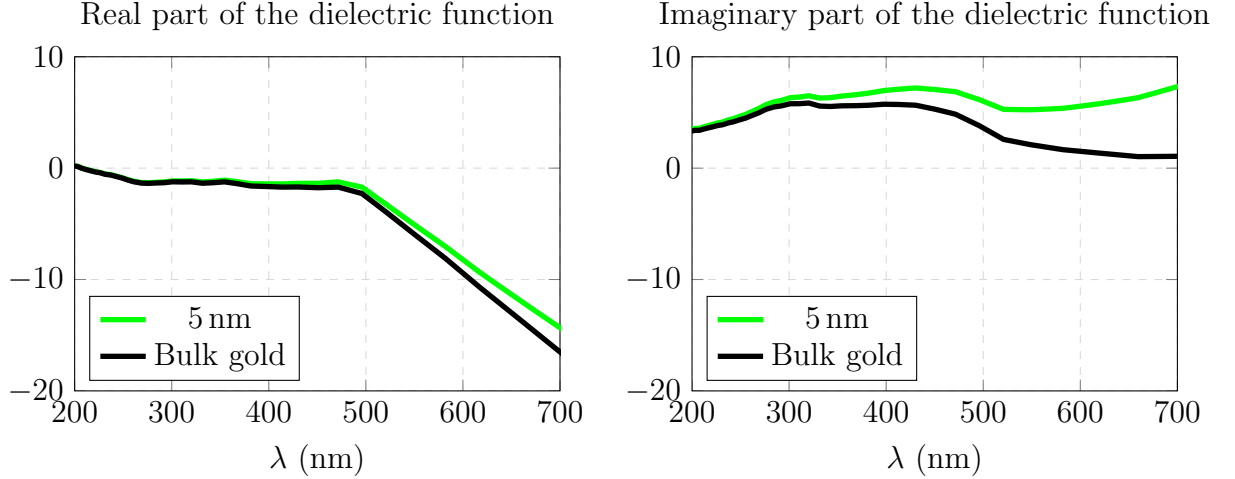$$\epsilon_{bulk} = \epsilon_{inter} + \epsilon_{intra}. \tag{3.15}$$

Figure 3.4: Comparison of the bulk dielectric function with the dielectric function corrected for small nanoparticles $\approx 5\,\mathrm{nm}$.

Electrons bound in the inner shells of the atoms undergo interband transitions to other unoccupied states. The electrons above the Fermi level are in the conduction band and they contribute to the dielectric function by the intraband transitions. These outermost electrons can absorb energy nearly as if they were free. Both parts of the ϵ_{bulk} are important to determine the position of the SPR, but in case of the size dependent damping, the Fermi electrons are usually assumed to be more sensitive.

To modify the dielectric function in the desired way, we want to keep the interband part of the bulk dielectric function unchanged and substitute the intraband part by the new term that includes the size dependent damping:

$$\epsilon_{intra}(\omega, a) = 1 - \frac{\omega_p^2}{\omega^2 + i\omega\gamma_0 + i\omega\gamma_A}. \tag{3.16}$$

The contribution of the free electrons to the dielectric function, ϵ_{intra}, can be described by the Drude model (3.9). The equation for the new dielectric function is:

$$\epsilon_{corrected}(\omega, a) = \epsilon_{bulk}^{exp}(\omega) - \epsilon_{intra}^{drude}(\omega) + \epsilon_{intra}(\omega, a). \tag{3.17}$$

Introducing the equations (3.9) and (3.16):

$$\epsilon_{corrected}(\omega, a) = \epsilon_{bulk}^{exp} + \frac{\omega_p^2}{\omega^2 + i\omega\gamma_0} - \frac{\omega_p^2}{\omega^2 + i\omega\gamma_0 + i\omega\gamma_A} \tag{3.18}$$

Figure 3.4 gives an example of the modification of the dielectric function for $L_{eff} = 5\text{nm}$. We can see that the real part of the dielectric function is less affected by the size effect, whereas the new imaginary part grows more rapidly, especially in the region of longer wavelengths. The material constants necessary for the correction, and their summary in comparison with other elements, is presented in Table 3.2. It is worth pointing out that the care should be taken in the choice of material constants. The values in the literature differ, for example those in [34] and [12], but they are usually close to the theoretical value predicted by the Drude model. However, this model omits the screening effect of the bound electrons. This screening is caused by the electron cloud around

Material	ω_p (eV)	$\omega_p(10^15s^{-1})$	γ_0 (eV)	$\gamma_0(10^15s^-1)$	$v_F(10^6$ m/s)
Silver	9.2	14	0.021	0.032	1.4
Gold	9.1	13.8	0.072	0.11	1.4
Copper	8.8	13.4	0.092	0.14	1.6

Table 3.2: Material constants for metals. Table reproduced from [34].

the positive cores. This negative charge reduces the force of the Coulombic attraction between the electron and the positive core, lowering the plasma frequency of the free electrons oscillations. The plasma frequency predicted by the Drude model may disagree with the experimental values [19]. For example, the theoretical value of the plasma frequency of silver is $\omega_p = 9.2$ eV, but the one measured experimentally as a minimum in the transmission curve of the parallel polarization of light is $3.78 \pm 0.02\,\mathrm{eV}$ [30]. This value, however, does not affect the profile of the spectra. More important is the damping constant which is responsible for the shape of the resonance peak.

Chapter 4

Software for simulation of the light-particle interaction

We have seen in Subsection 2.4 that for a spherical scatterer an analytic solution can be obtained. The complexity of this derivation also indicates difficulties one will encounter when some more general, for example a polyhedral shape should be treated analytically. However, irregular shapes occur frequently in nature. It is the consequence of higher energetic stability of particularly oriented faces. It will be shown in Section **??** that the growing nano-crystals tend to form polyhedral shapes bound with facets of specific crystallographic orientations. In the technological applications, we wish to fabricate nanostructures with geometry predefined by their purpose. Plasmonic antennas can be an example of such structures [35].

To predict optical properties of geometries different from spherical and ellipsoidal ones, we have to reach for approximative, numerical calculations. We will present two of the methods used in simulations of optical response of nanostructures. The first method is the Finite difference time-domain technique (FDTD), which uses the finite elements approach. This method is implemented in the FDTD Solutions software. The other method used for solution of scattering problems is the so called Discrete dipole approximation (DDA) [36]. In this approach, the object is divided into discrete subvolumes. The second technique is implemented by an open source program DDSCAT developed specifically for solving electromagnetic scattering by the particles of arbitrary shapes. We will describe the principles of both methods in this chapter.

4.1. Discrete Dipole Approximation

The DDA method (sometimes also referred to as Coupled Dipole Method – CDM) was first presented by Purcel and Penypacker [37] in 1973. The area occupied by a scatterer is divided into an array of discrete polarizable entities. External electromagnetic field induces the dipole moments in every point occupied by the entity. In principle, each dipole interacts with the incident field and the field from surrounding dipoles. This interaction produces the system of linear equations. The solution of the system gives the polarizability which carries the information necessary for determining the scattering properties of the object under study.

4.1. DISCRETE DIPOLE APPROXIMATION

Since 1988, DDA has been subjected to series of improvements mainly by Draine and coworkers. Draine and Flatau wrote an open source Fortran code DDSCAT which implements the discrete dipole approximation. An overview of its features can be found in the review article [38]. The software takes advantage of the algorithms that speed up the calculations. This allows using a relatively high number of polarizable points N and, at the same time, maintains reasonable computing time. Such improvements make DDSCAT a powerful tool also for plasmonic simulations of the particles of nanometer sizes.

The manual for DDSCAT 7.2 [39] states the conditions of validity. It requires the interdipole separation d to be less than any structural length of the target and less than the wavelength of the used light. Thus for accurate calculations the parameters should satisfy

$$|m|kd \ll 0.5, \tag{4.1}$$

where m is the complex index of refraction, d the interdipole separation, and k the wavenumber. The recommended interval in which DDA is valid is set to be $|m| < 2$. DDSCAT is suitable neither for very high values of index of refraction nor for large particles. However, high values of $\mathrm{Im}\{m\}$ can be compensated by lowering the interdipole separation.

More complex geometries of the studied particles lead to more complicated behavior of the field, such as in the vicinity of vertices, or at the points close to the area where objects touch each other. The amount of dipoles must be adequate to represent all the geometrical features of the desired shape. This can be tricky for the shapes that are better represented in other coordinate systems, as the rectangular coordinate system is the only one that can be used for the reasons stated below. The example of the quality of the shape approximation is shown in figure 4.1. The more complicated the geometry, the more careful we have to be regarding the number of dipoles we use in our simulation. On the other hand, for objects with the cubic symmetry, the accurate results can be obtained with considerably smaller N.
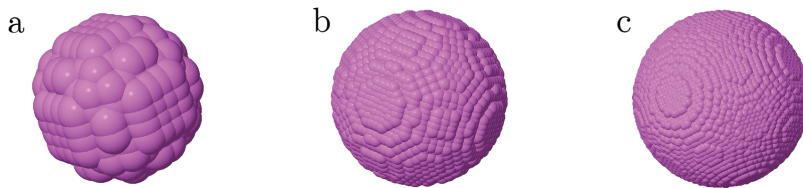

Figure 4.1: Sphere constructed of the arrays of dipoles. For the purpose of illustration, the dipoles are depicted as beads. In the model, the points and the subvolumes are not overlapping. The shape approximation using a)$N = 552$, b)$N = 14.328$ and c)$N = 65.754$ points is shown.

The program itself generates many pre-defined shapes, see [39, p. 34] or allows straightforward implementation of any user defined shape. DDSCAT has routines for treating finite targets or their infinite arrays.

4. SOFTWARE FOR SIMULATION OF THE LIGHT-PARTICLE INTERACTION

The central equation solved by the DDA method is

$$\mathbf{E}_i = \mathbf{E}_i^{inc} + \sum_{j \neq i} \overline{\mathbf{G}}_{ij} V_j \chi_j \mathbf{E}_j + (\overline{\mathbf{M}}_i - \overline{\mathbf{L}}_i) \chi_i \mathbf{E}_i, \tag{4.2}$$

where $\mathbf{E}_i$ stands for the net electric field, $\mathbf{E}_i^{inc}$ is the electric intensity of incoming field, χ is the susceptibility of the material, V is the volume that contains the point with certain susceptibility, $\overline{\mathbf{G}}_{ij}$ is the dyadic Green's function. The functions $\overline{\mathbf{L}}_i$ and $\overline{\mathbf{M}}_i$ are the functions defined via integrals over the area corresponding to a subvolume. $\overline{\mathbf{L}}_i$ is only a function of the subvolume geometry and does not depend on the cell size. On the contrary, $\overline{\mathbf{M}}_i$ only depends on the cell size. The usual approximation approach is to take the susceptibility and electric field constant in each subvolume.

$$\mathbf{E(r)} = \mathbf{E}_i, \qquad \chi(\mathbf{r}) = \chi_i \qquad \text{for } \mathbf{r} \in V_i, \tag{4.3}$$

The simplest formulation of the problem to be solved by DDA is the equation

$$\mathbf{E}_i^{inc} = \overline{\alpha}_i^{-1} \mathbf{P}_i - \sum_{j \neq i} \overline{\mathbf{G}}_{ij} \mathbf{P}_j, \tag{4.4}$$

with the polarizations P_i given by

$$\mathbf{P}_i = \overline{\alpha}_i \mathbf{E}_i^{exc} = V_i \chi_i \mathbf{E}_i. \tag{4.5}$$

The polarizability α_i of a single dipole is often defined by the Clausius–Mossotti relation, which arises from the Maxwell equations for an ideal dielectric:

$$\alpha = \frac{3d^3}{4\pi} \frac{m_i^2 - 1}{m_i^2 + 2}. \tag{4.6}$$

Draine and Goodman [40] derived a more exact equation based on a dispersion relation for an infinite array of lattice points. The polarizability used in DDSCAT is based on this so called Lattice Dispersion Relation (LDR) and yields better results even for higher refractive indices [41]. Equation (4.5) is exact only as far as the assumption (4.3) holds. Taking the field and susceptibility constant within the cell gives rise to discretization and the shape approximation errors. Generally, both errors are reduced when $N \to \infty$ for the fixed geometry and size of the object. The errors are not decreased in the long-wavelengths region, i.e. when $kd \to 0$ at fixed N because DDA tends to overestimate the surface polarization and is therefore inaccurate. We have to point out that the above described discretization in the DDA is the only approximation and the problem is then solved essentially exactly.

The chosen numerical algorithms are of a crucial importance as they can greatly reduce storage and computing demands. Among others, the Block–Toepitz matrix is used to find the symmetry in the interaction matrix, making the following computations less demanding and the storage easier. The Fast Fourier transform converts multiplication of the interaction matrix to the discrete convolution, making the process faster, but it requires that the whole computation is done in rectangular coordinate system.

4.2. Finite-Difference Time Domain Method

Finite elements methods are used in many fields of physics where mathematical conditions give rise to the systems of differential equations. The differential equations are solved as difference problems by the so called leapfrog method, i.e. the step-by-step numerical integration. In this work, we employed a commercial software package FTDT Solutions by Lumerical. The simulation is in *time domain*, which means that the algorithm computes the time development of the signal and then, using the Fourier transform, the frequency dependence can be obtained. Solving the problem in time domain means handling the set of frequencies in one simulation. FDTD can solve problems for complicated geometries of the samples as well as for nonlinear materials.

The method is discrete both in time and space. The volume containing the scatterer and its surroundings is divided in so-called Yee cells forming the rectangular mesh.
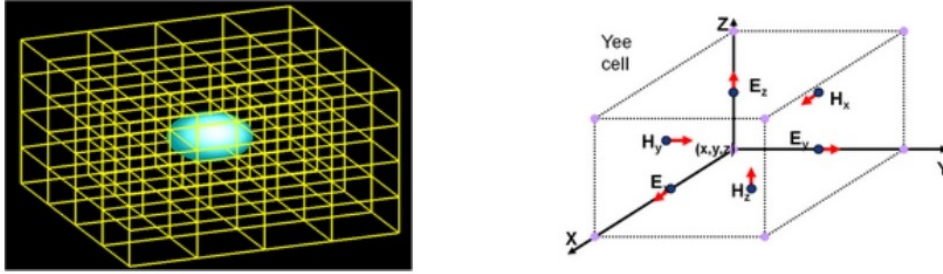
Figure 4.2: The space divided into rectangular subvolumes, forming the mesh. A single Yee cell is depicted on the right.

FDTD methods solve directly the time dependent Maxwell equations

$$\nabla \times \mathbf{E} = -\mu_0 \frac{\partial \mathbf{H}}{\partial t}, \tag{4.7}$$

$$\nabla \times \mathbf{H} = -\epsilon\epsilon_r \frac{\partial \mathbf{E}}{\partial t}. \tag{4.8}$$

Equations are rewrited into the difference form and solved using the *Yee algorithm*. In every step, either electric or magnetic field is calculated in the iterative steps. The Yee cells obey special ordering where every $\mathbf{E}$ component is surrounded by four $\mathbf{H}$ components (see Figure 4.2). For every cell, $\mathbf{E}$ field is calculated using the previous value of $\mathbf{H}$. Then $\mathbf{H}$ field is calculated from $\mathbf{E}$. Both fields are linked to each other via rotations and the calculation ends when a steady state is reached.

One of the problems of FDTD method is that we have to introduce some artificial conditions for the borders of our computational space. Some strongly absorbing material is added and it also needs to be discretized, which increases the computational demands of the problem. Operating the mesh is a little less variable as the finer discretization often has to be done over entire simulation space.

To get the desired information about the properties of the scatterer, we need to place frequency-domain profile monitors into the vicinity of the object. The monitors collect information about the field by calculating the flux of Poynting vector or the flux of the

power through them. Then frequency dependences can be derived and plotted. The program offers sample dielectric functions and predefined geometries as well as the possibility to create new ones. Also dielectric functions defined by the user can be imported. Every imported set of values has to be fitted to obtain an analytical expression. This is often done by adding Lorentzian terms to the Drude model [42],

$$\epsilon(\omega) = \epsilon_{Drude} + \sum_{j=1}^{k} \frac{f_j \omega_j^2}{(\omega_j^2 - \omega^2) - i\omega\gamma_j}, \tag{4.9}$$

where ω_j and γ_j are the oscillator resonant frequency and damping constant, respectively, and f_j are the weighting factors. Nonetheless, the fit may struggle to reproduce the slight variations in the interval of interband transitions or the sharp absorption edges.

Chapter 5

Measurement and simulations

5.1. Experimental settings

For the purposes of optical spectroscopy enabling transmission, reflection and photoluminiscence experiments on colloidal samples a special apparatus has been designed and assembled in the Institute of Physical Engineering (IPE) at Brno University of Technology. Its schematic is depicted in Figure 5.1.
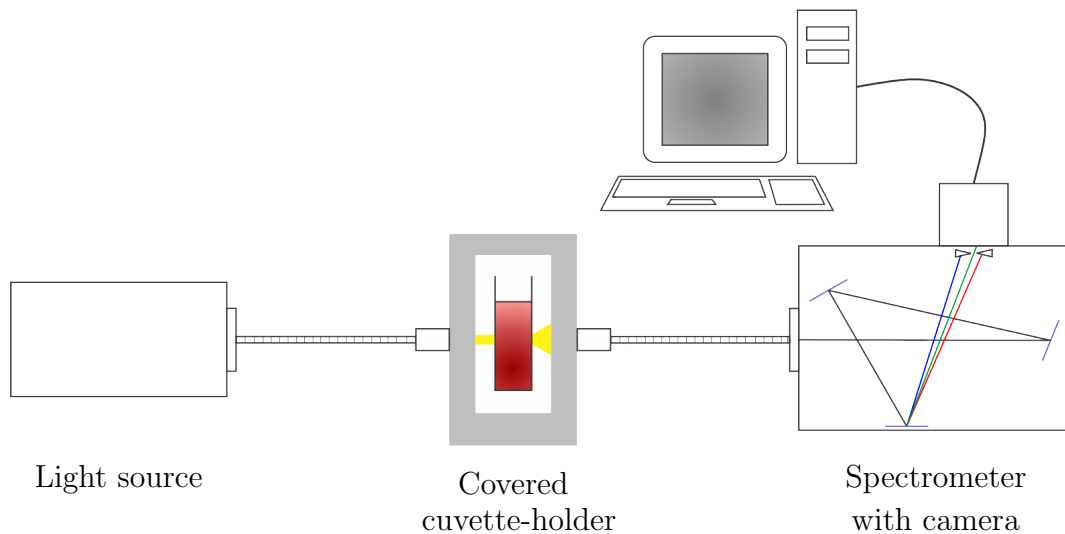
Figure 5.1: Schematic of the apparatus for optical spectroscopy on colloidal samples.

The source of light is a halogen-deuterium lamp DH2000 (Avantes). The lamp provides illumination in the range of wavelengths from the ultraviolet to the near infrared. We used the Czerny-Turner spectrometer Shamrock SR-303i produced by Andor Technology with a wavelength resolution of 0.1 nm. The camera iDUS 420BU with a back-illuminated CCD chip and 1024x256 active pixels suitable for fast data acquisition served for the detection.

The light in the apparatus passes through the sample holder where a cuvette with a reference sample without nanoparticles, typically distilled water is placed. In this way, the reference spectrum is obtained. Then the measurement is done for a studied sample in the form of a colloidal solution in the cuvette. The intensities measured for the actual sample

are further called the signal. We are interested in extinction, thus the acquisition mode of the camera software is chosen to recalculate the measured signal using the following equation:

$$Q_{ext} = A \times \left(1 - \frac{\text{Signal} - \text{Background}}{\text{Reference}} \right), \tag{5.1}$$

where the background is the dark current, i.e. the signal measured when the slits of the spectrometer are closed and A is the normalization constant. Normalization is done with respect to the maximum value of the resonance peak in order to make the data comparable. The background signal and the reference are valid for specific ambient conditions affecting the apparatus, e.g. external sources of light or temperature, and for the given acquisition interval of wavelengths. If any of this parameters is changed, the reference and background should be measured again.

Analysis of the nanoparticles, was done by scanning electron microscopes Vega and Lyra (TESCAN). To confirm the composition of the samples, the particles of dimensions 20 nm and larger were examined by the observation in SEM. The smaller particles are not convenient for the size and shape analysis by this method, as their dimensions are comparable to the spot-size of the primary beam and their contours thus become unclear.
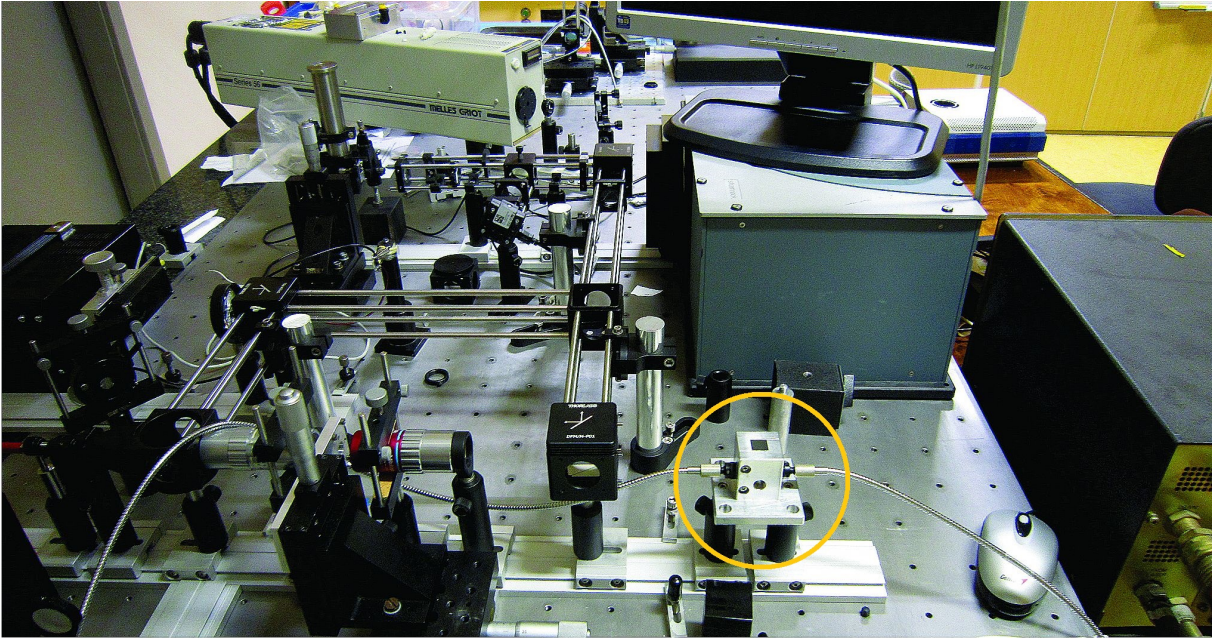
Figure 5.2: Aparatus for optical spectroscopy. In the foreground, the cuvette holder for measurements of colloidal solutions is noticeable (yellow circle). Light is led into and out of the cuvette by the optical fibers.

5.2. Gold nanospheres in colloidal solutions

In this Section, we present the results obtained by measurements of light extinction caused by colloidal nanoparticles and the corresponding numerical calculations. We began our study with spherical particles, as their optical response can be accurately predicted using the Mie theory, thus representing a good starting point for further investigations.

We used the freely available program MiePlot 4.3 to calculate the extinction efficiency spectra. Comparison of the Mie spectra with the experimentally measured ones helps us to validate the composition of the measured sample. SEM analysis also provides a good information about the composition of the samples, considering the uniformity of the diameter of the studied nanospheres and the presence of the shape deviations. However, we are restricted to a small fraction of the total amount of particles contributing to the scattering. Then we look for the optimal parameters of numerical calculations independently of the Mie result. The condition of validity is the stability of solution as a function of the density of the mesh for FDTD method and the number of dipoles for the DDA. When the stability is reached, i.e. we have determined the region of discretization that gives us similar results, the calculated spectra should correspond to the experimental ones.

As the samples we used commercially available colloidal solutions of golden nanoparticles produced by BBI Solutions. The product should be a solution of nanoparticles with 95% of them having the spherical shape and with the coefficient of variation of the size distribution (i.e. the standard deviation from the mean diameter) equal to 8%. The solutions have the concentration of 10^7 particles per ml and the particles were passivated by a sodium citrate capping layer to prevent them from aggregation. Before the measurement, all solutions were dissolved by adding distilled water in the ratio 1:2 (colloidal solution : distilled water). We examined samples with diameters of 5, 10, 20, 40, 80, 100 and 150 nm.

The presented micrographs, Figures 5.3 - 5.8, were obtained by exposing a silicon substrate (On Semiconductor) to the colloidal solution for 4 hours. By analyzing them, we obtained the statistics of the size distribution of colloidal nanoparticles in the sample, with exception of the samples containing nanospheres of 10 and 5 nm in diameter. The statistics, presented in Table 5.1 also lists the corresponding experimental resonance frequencies. The values and errors of λ_{res} were extrapolated by fitting.

Diameter	$\bar{d}$ (nm)	Std. dev. (nm)	λ_{res} (nm)	$\Delta \lambda_{res}$ (nm)	FWHM (nm)
150	153.63	10.01	683.99	2.30	669.17
100	98.55	5.66	573.20	0.50	378.50
80	80.40	5.82	549.14	0.23	268.44
60	60.93	5.24	532.24	0.20	196.67
40	41.03	2.72	521.89	0.27	155.44
20	21.06	1.27	517.23	0.54	189.50
10	–	–	511.30	0.44	227.56
5	–	–	513.41	0.41	264.08

Table 5.1: Gold nanospheres in colloidal solutions. The diameter corresponds to the size stated by the manufacturer. The table shows $\bar{d}$ – average diameter measured by SEM, standard deviation of the d, resonance wavelength λ_{res} and related error, full width of the resonance peak in half-maximum.
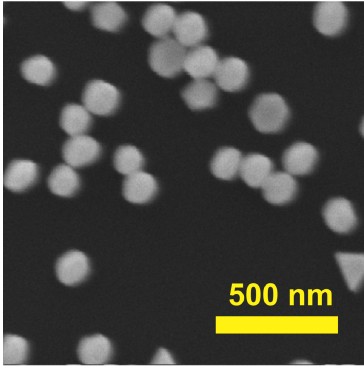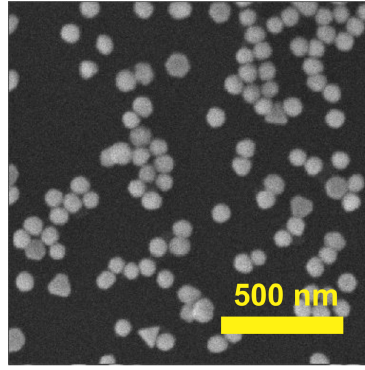
Figure 5.3: d = 150 nm   Figure 5.4: d = 100 nm   Figure 5.5: d = 80 nm
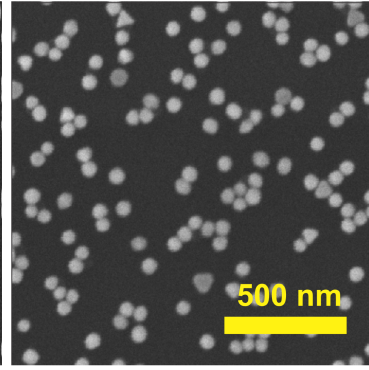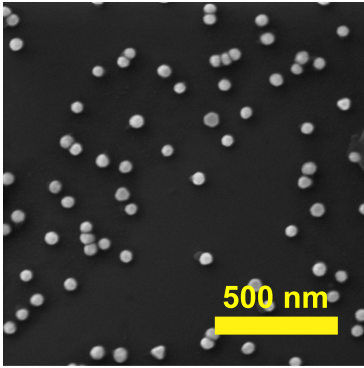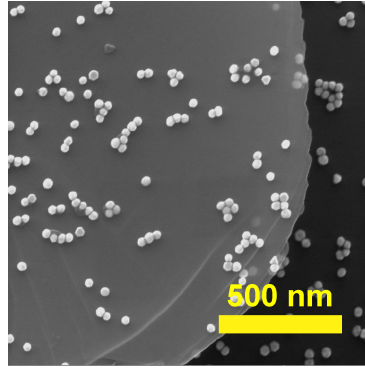
Figure 5.6: d = 60 nm   Figure 5.7: d = 40 nm   Figure 5.8: d = 20 nm
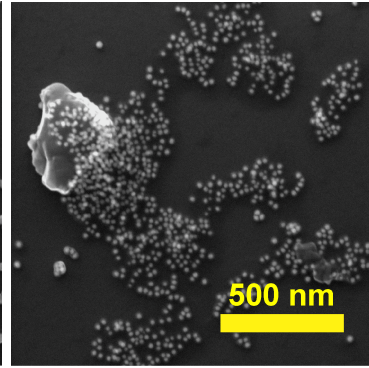
The values of the standard deviation of the diameter d in Table 5.1 indicate that the size difference of a nnoparticles in the colloidal solution varies in the range of several units of per cent. Therefore, the simulations carried out for uniform samples should pose a good model for these solutions. The graphs in Figure 5.8b show experimental and theoretical results of the extinction factor defined by relation (2.12). In the low energy tail of the extinction peaks, we can observe a slight difference from the Lorentz curve for the spheres from 80 to 150 nm. Instead, the decrease in intensity appears to be more linear. This indicates an increased damping which is an effect of the size of the particle. At these sizes not all electrons in the particle volume feel the same field and thus, the force driving

their resonance is not the same over the volume. This non-coherence in the oscillations leads to the accumulation of charge and acts as another source of damping [15]. For the nanoparticle dimensions approximately 60 nm and higher, the surface-effect correction of the dielectric function mentioned above has nearly no effect and the only damping is that of the bulk material characterized by γ_0. This corresponds to the value of the mean free path of conduction electrons in gold which is approximately 40 nm [43]. On the contrary, the agreement of the experimental spectra with the DDA and Mie simulations for the small sizes was achieved by correcting the dielectric function. We used the values ω_p=8.55 eV, γ_A=0.1077 eV and v_F=1.4 × 10^6 m/s and appropriate value of γ_A, calculated from the equation (3.13).

The deviation of the curve obtained by the FDTD from the other curves, is most probably caused by the fact that the mesh constant has to be found carefully for each size of the modeled sphere. For the sizes 20 nm and less, mesh spacing lower than 1 nm has been used. Finer discretization increases computational demands greatly. For the diameters 40 nm and less, we observed the presence and growth of another peak centered over 700 nm. This peak is most probably caused by the shape approximation error. The ideal spherical shape is lost without the minute spacing of the mesh points. This attribute is the biggest difference between the FDTD prediction and the other data.

The calculations done with DDSCAT were done with approximately 10^5 dipoles approximating the spherical shape for all sizes of spheres we have studied. The computational time was in all cases roughly in the units of hours. In the FDTD calculations, we were able to obtain accurate spectra of particles larger than 40 nm with relatively rough mesh spacing. For smaller sizes, the rough mesh spacing lead to big errors in the results. Simple increase of mesh points was not generally sufficient to obtain accurate results. Several calculations had to be made to find the correct mesh spacing. The computational time is not easy to compare as both techniques utilize memory and processor of the computer differently. But for both techniques the accurate calculations with high number of dipoles or fine mesh spacing should not exceed tens of hours, on the available computational machine.
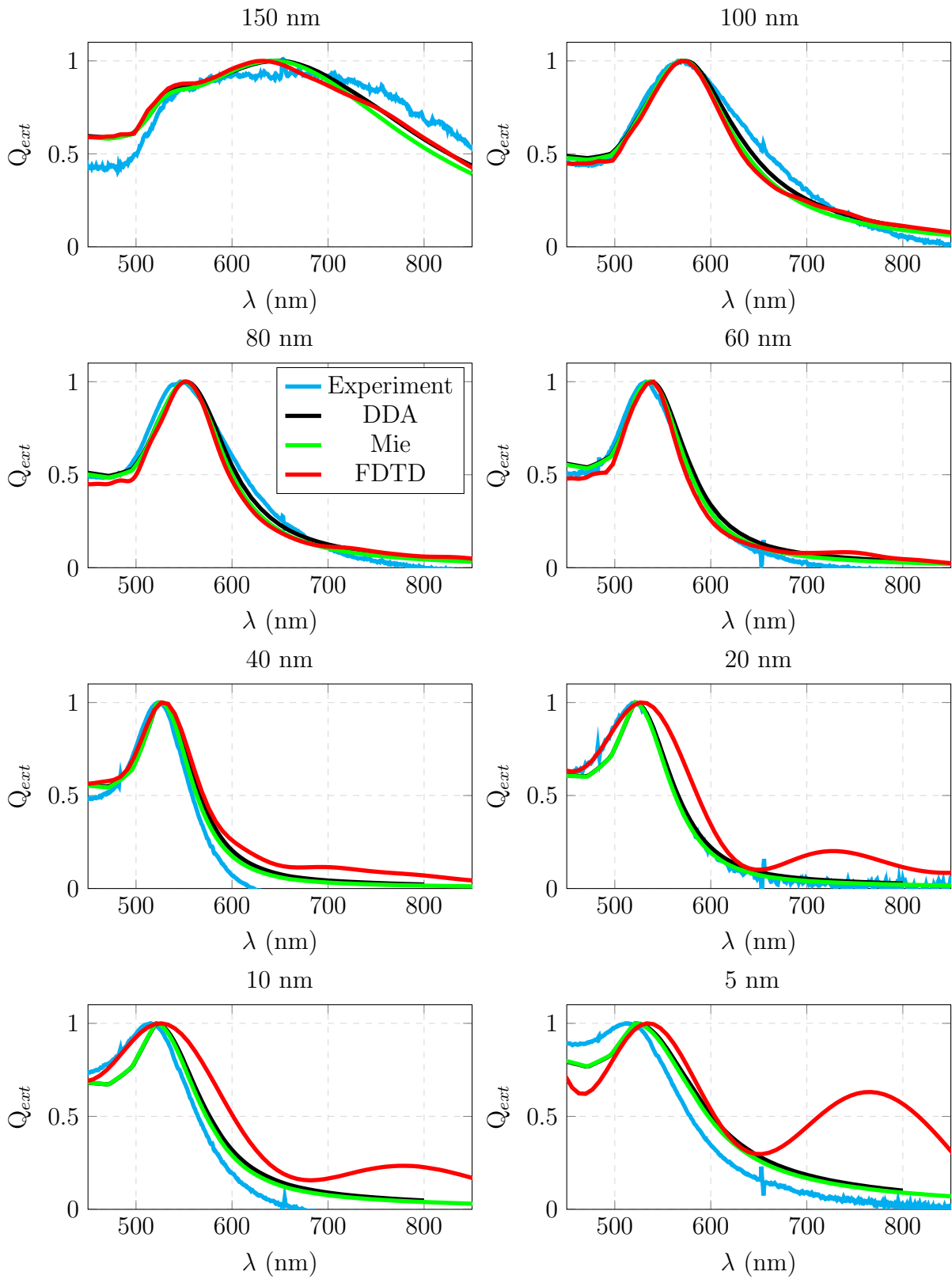
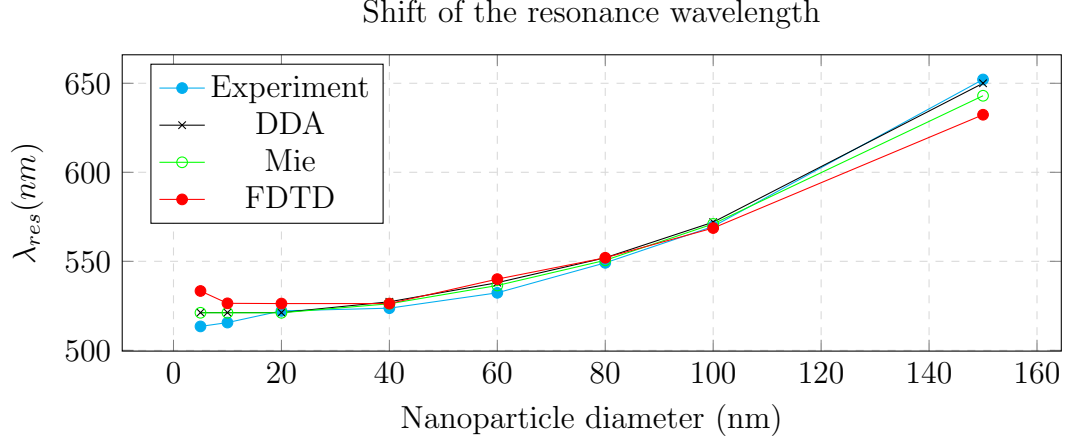Figure 5.8b: Optical spectra of spherical colloidal nanoparticles. Data were normalized.

Figure 5.9: Comparison of the experimental and simulated dependences of resonance wavelengths of the nanoparticles on their diameter.
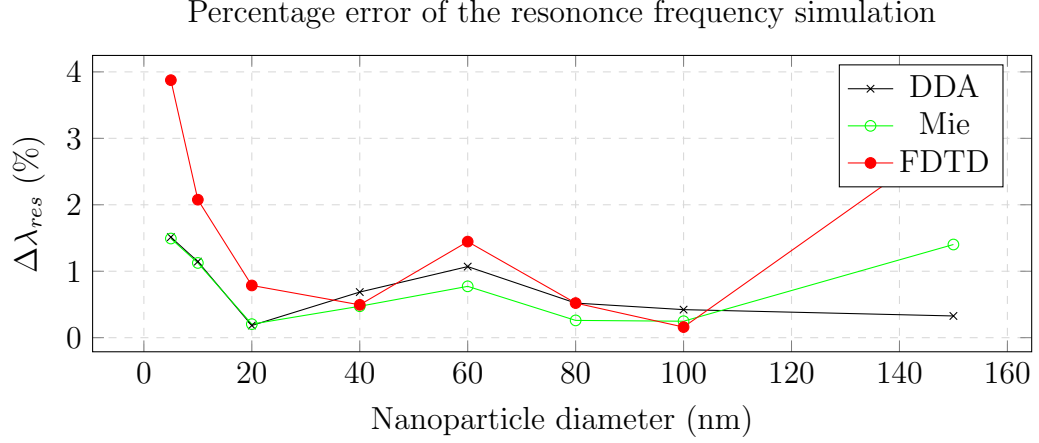

Figure 5.10: Relative deviation of simulated resonance wavelengths (in per cents) from those obtained experimentally as a function of particle diameter.

Further comparison of the results obtained experimentally and by various simulation methods for different particle diameters is given in Fig. 5.9. There is a noticeable nonlinear red-shift of the resonance wavelength of the nanoparticles with their increasing diameter. The resonance wavelengths calculated by DDA are in a good agreement even for diameters below 20 nm, where some deviations from the experiment and Mie solution were observed (considering the peak profile). For the small particles below 20 nm, FDTD gives less accurate results than the DDA does. Resonance wavelengths given by FDTD for the sizes 5 nm and 10 nm are in good agreement, although the peak profile obtained by FDTD deviates strongly from the other data. This difference results clearly from the effect of particle approximation by the rectangular Yee-cells. The relative deviations of simulated resonance wavelengths in per cents from those obtained experimentally as a function of the particle diameter are shown in figure 5.10. We can see the largest deviations for the marginal values of our interval of interest. However, the level of noise in the measurement of the 150 nm sample may have influenced the data extrapolation and the result may not be as accurate as the other ones, see Table 5.1.

5.3. Synthesis of Gold Nanorods

During the past few years, many techniques have been investigated and applied to produce NPs of well-defined shapes and sizes. Among others, the Turkevich recipe [44], the Stucky method [45] or the Frens method [46] which controls the size of synthesized nanoclusters by the concentration of sodium citrate. Preparation of rhombohedral nanoparticles by photo-chemical polythiol reaction was reported [47] as well. The synthesis of anizotropic particles is the subject of a deep interest. There are electrochemical methods [48], the seed-mediated growth methods that require the primary "seed" solution and stimulate the anizotropic growth in the second step [49, 50], or even seedless method [51].

The common step of the "seeded" chemical processes of the synthesis is the initial strong reduction of a metal salt producing single crystalline "seeds". The reactants and their concentrations vary. For the further growth, more metal salts are added and the growth takes place at the presence of a weaker reducing agent than in the first part. For controlling the shape, tamplates [52] or structure-directing agents [53] can be used.

The fabriaction of nanoparticles is not only limited to chemical methods, for instance, laser ablation in an aqueous solution leads to the production of nanoparticles as well [54]. In principle, the methods like electron beam litography (EBL) or milling by focused ion beam (FIB) can also produce nanoparticles or nanostructures.

The advantage of chemical ways of fabrication of nanoparticles is their relatively high efficiency. On the other hand the nonuniformity of the prepared sample, common for this method, is a limiting factor which is, however, being continuously reduced by the development of novel procedures of the synthesis.

The purpose of the study presented in the previous section was to provide comparison of the available measurement technique with the simulation methods in order to characterize the samples of colloidal gold nanoparticles. In this part, our goal was to investigate the applicability of these methods to the control of the chemical synthesis of gold nanorods.

In the synthesis, we followed the procedure presented in the paper written by Sau and Murphy [50]. In this way, short gold nanorods (GNR) are synthetized at a high yield. Figure 5.11 gives a schematic view of the process.
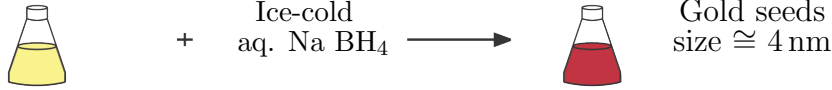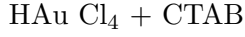
5.3.1. Process of synthesis

For the synthesis the following chemicals were purchased from the Sigma-Aldrich company: $H\,Au\,Cl_4$ (99%), $Na\,BH_4$ (99%), ascorbic acid (99%), cetyltrimethylammonium bromide (99%) and $Ag\,NO_3$ (99+%). To dissolve the chemicals, deionized water was used. The steps are schematically depicted in figure 5.11

First, the **seed solution** was prepared. The 1.25 ml of an aqueous 0.01 M solution of $H\,AuCl_4 \cdot 3H_2O$ was added to 37.5 ml of a 0.1 M cetyltrimethylammonium bromide (CTAB) solution. During the mixing, the solution turned its color to orange-brown. Then the 3 ml of aqueous 0.01 M ice-cold $NaBH_4$ were added while the solution was rapidly mixed. The whole solution was then put into a water bath where it was maintained at $25\,°C$. The seed solution, kept in stable conditions, can be stored for up to one month [50].
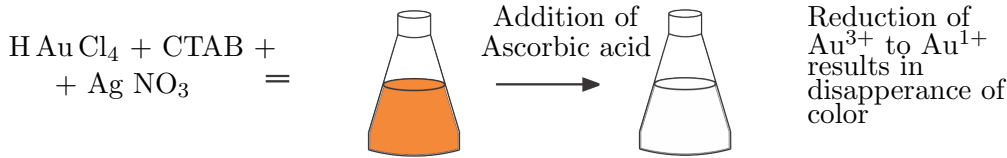
Secondly, the **stock solution** was prepared. $HAuCl_4$ was mixed together with $AgNO_3$ in an aqueous solution of 9.5×10^{-2}M CTAB. The primary concentration of Au^{3+} was 4.0×10^{-4} M and Ag^+ had a concentration of 6.0×10^{-5} M. The solution in this stage has deep orange color. Then ascorbic acid (AA) was added with a concentration of 6.4×10^{-4} M. AA serves as a reducing agent and changes the oxidation state of Au^{3+} to Au^{1+}. This reaction leads to the disappearance of color of the solution.

I. Synthesis of seed

$HAuCl_4$ + CTAB

Ice-cold
aq. $NaBH_4$

Gold seeds
size $\cong 4$ nm

II. Stock solution

$HAuCl_4$ + CTAB +
+ $AgNO_3$ =

Addition of
Ascorbic acid

Reduction of
Au^{3+} to Au^{1+}
results in
disapperance of
color

III. Nanorod synthesis

;

Seed + Stock
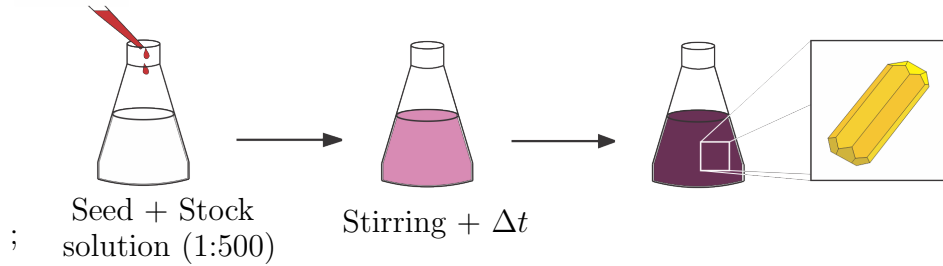solution (1:500)

Stirring + Δt

Figure 5.11: Seed-mediated process of synthesis of gold nanorods with the controlled aspect ratio. This approach leads to fabrication of nanorods of a high aspect ratio. Figure reproduced from [53].

Finally, the stock solution and seed solution were mixed in the last step producing the substance where the growth of gold nanorods is facilitated. 0.5 ml of the seed solution was added to 250 ml of the stock solution. The final growth of nanorods took place under continuous stirring at room temperature. The color change of the solution is shown in figure 5.12.

5.3.2. Characterization of gold nanorods

First, we present the DDA simulations of optical response of gold nanorods as a function of their aspect ratio. As a model of the nanorod, we used a rectangular prism. Previous experiments with modeling colloidal solutions of nanospheres have confirmed the assumption that the ambient medium in colloidal solution is similar to water, i.e. $N = 1.33$. Although we have considered the light interaction with a randomly oriented prism in our simulations, we have not found an increase of the extinction efficiency, corresponding to the transversal plasmon resonance, similar to the experiment. For the polarization
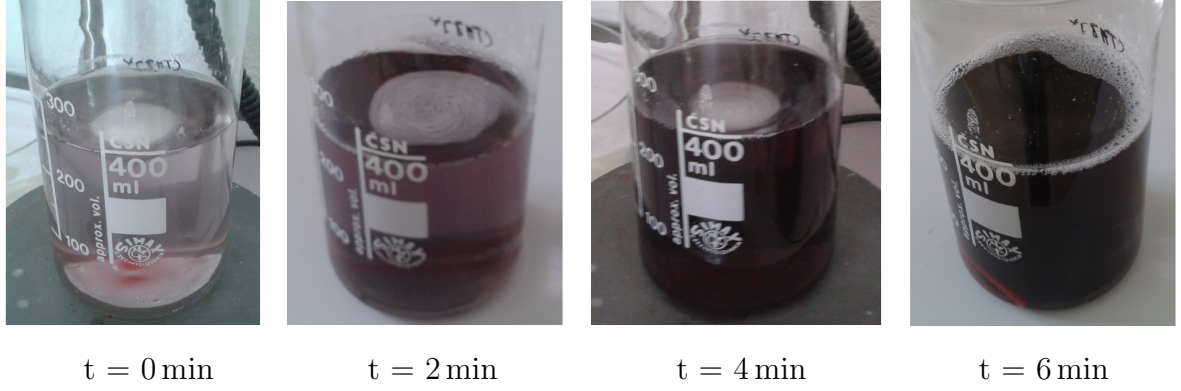
| t = 0 min | t = 2 min | t = 4 min | t = 6 min |

Figure 5.12: Evolution of color of the solution. At $t = 0$ the seeds were added to the stock solution. We can see the color getting darker as the nanorods grow in length.

oriented perpendicularly to the main axis of the rod, the intensity and width (not the position) of the main peak in the simulations is changed, but not decreased markedly in favor of the transversal resonance maximum.

The absence of the transversal plasmon resonance can be explained by a large variety of orientations that is presented in the sample. Probably, by careful orientation-averaging, the transversal resonance should appear in a summation over the spectra. The effect of the cross-sectional shape of the rod may also play a role in the shape of the spectrum, but it should not suppress it. Although it may seem that the cross-sectional geometry of the rod affects the transversal resonance preferentially, our results have shown the longitudinal resonance being affected considerably.

The position of the longitudinal resonance wavelength red-shifts with an increasing aspect ratio. The transversal resonance can be located at the wavelengths close to 520 nm and its intensity decreases rapidly as the aspect ratio gets bigger.

Our simulations (Figures 5.13 and 5.14) indicate the linear dependence of the position of the resonance on the aspect ratio. However, the study over a wider interval of aspect ratios should be done to confirm this observation.

Scanning electron micrographs were taken to confirm the composition of the measured colloidal solutions. Instead of putting the silicon sample into the solution, pippeting a droplet on a silicon surface gives better coverage of the sample. This simple method also does not critically affect the chemical stability of the nanoparticle capping layer during segregation. Although the particles tend to coalesce, they do not form new clusters.

The nanorods, depicted in Figure 5.15, were synthesized by RNDr. Michaela Šimšíková, Ph.D., by the process described in Section 5.3.1, with the desired dimensions approximately 40 nm × 90 nm. The solution containing nanorods shown in figure 5.16 was kindly provided by Ing. Filip Novotný from the Faculty of Nuclear Sciences and Physical Engineering at the Czech Technical University in Prague. The samples depicted in Figures 5.17 and 5.18 are the bare gold nanorods produced by the Nanopartz company. The stated dimensions of the nanorods are 10 × 38 nanometers with the SP resonance at 780 nm (Figure 5.17) and 10 × 45 nm with the main resonance at 850 nm (Figure 5.18).
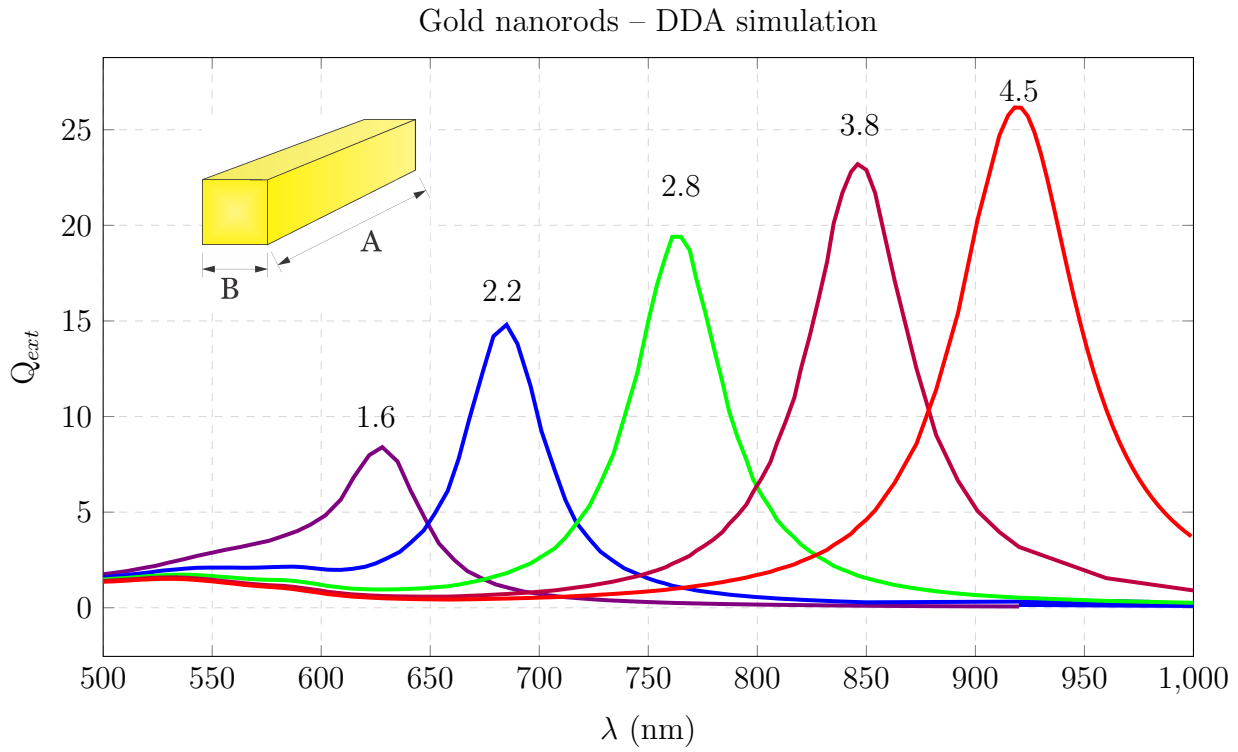
Figure 5.13: Simulated (DDA) extinction efficiency as a function of the changing aspect ration of gold nanorods. The numbers over the maxima denote the corresponding aspect ratio A/B, as labeled in the upper-left part of the scheme.
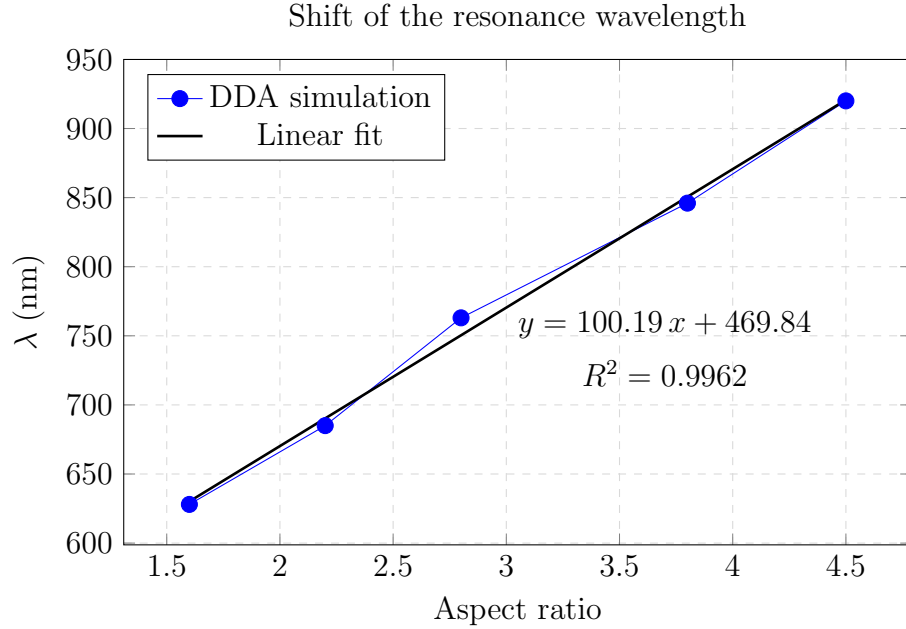

Figure 5.14: Gold nanorods. Dependence of the simulated resonance wavelength on the aspect ratio of the illuminated sample. The resonance frequency corresponds to the longitudinal plasmon mode. Results calculated by DDA.
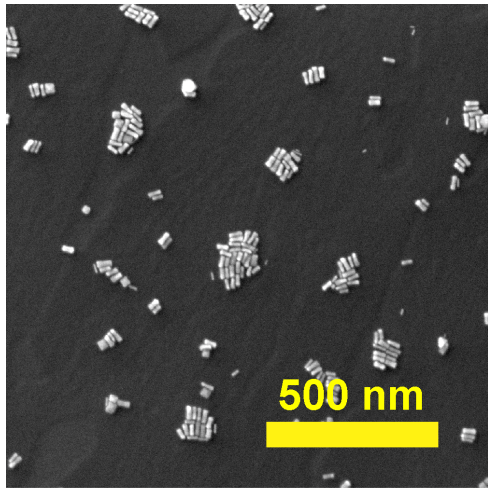
Figure 5.15: Gold nanorods on silicon substrate. Aspect ratio 2.8.
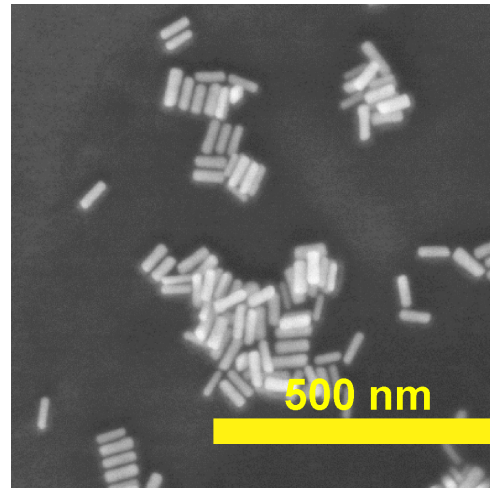

Figure 5.16: Gold nanorods on silicon substrate. Aspect ratio 3.
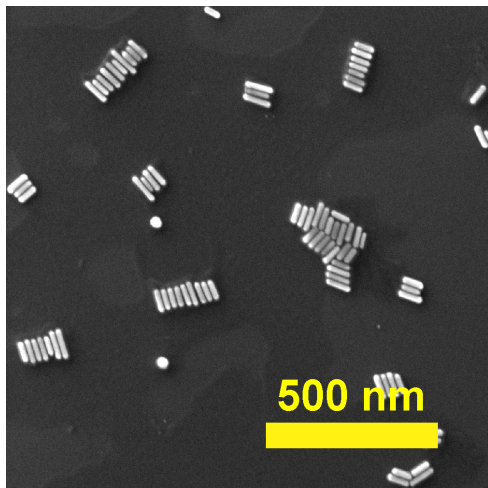

Figure 5.17: Gold nanorods on silicon substrate. Aspect ratio 4.
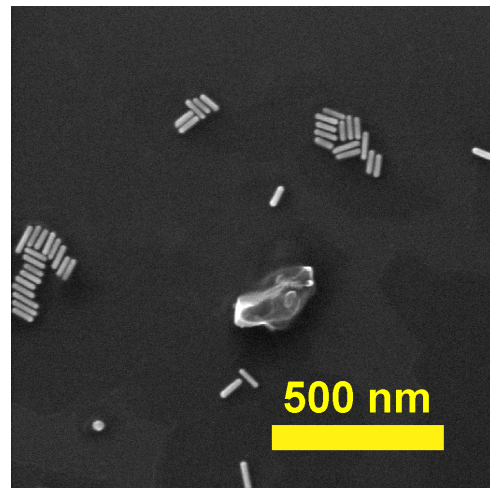

Figure 5.18: Gold nanorods on silicon substrate. Aspect ratio 4.8.

The spectra for colloidal nanoparticles (Figure 5.19) were measured using the same procedure and the same apparatus as described in Section 5.1.
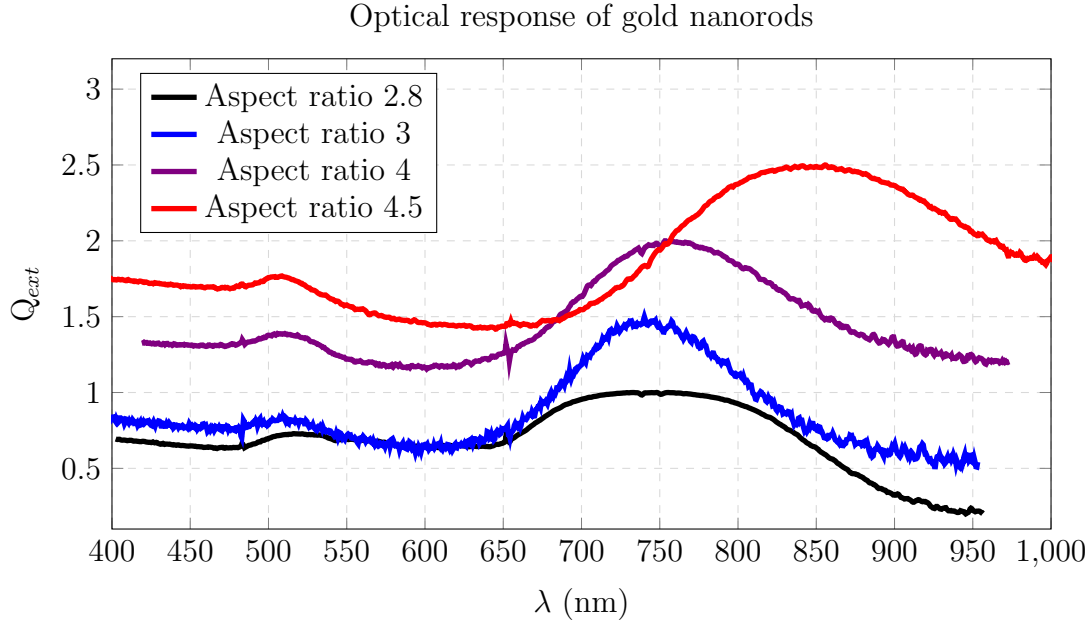
Figure 5.19: Experimentally measured extinction efficiencies for gold nanorods of different aspect ratios. The transverse resonance mode shifts slightly around the wavelength 520 nm. The shift of the longitudinal resonance mode located above 700 nm is significant.
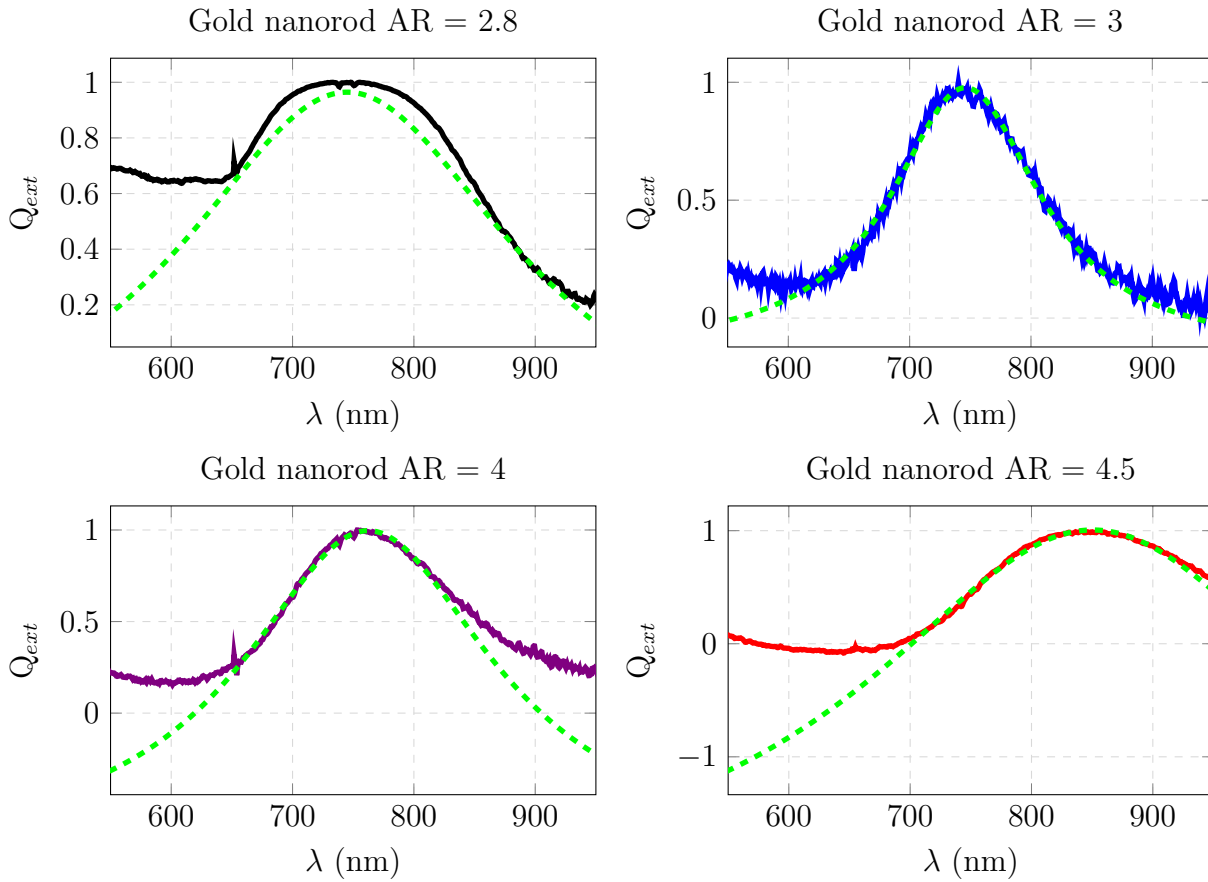

Figure 5.19b: Experimental extinction spectra. Solid lines correspond to the experimental data. Dashed lines represent fitting by the Lorentz functions.

The simulation results for the rectangular nanorods do not correspond to the measurements of those with the same aspect ratio – the resonance frequency in the simulations grows faster with an increasing aspect ratio than in the experiment, see Table 5.2. The details of the fitted data are depicted in figure 5.19b. Other morphologies were studied theoretically as well, to investigate the effect of cross-sectional geometry of the rod on the resonance shift, see Fig. 5.20. Octagonal rods and prolates were simulated by the DDA method. The results indicate that the shape of the rod has a crucial impact on the behavior of longitudinal resonance. The octagonal rod has a simple shape without any truncation at the ends. The prolate rod is an ellipsioidal body, with two semiaxes of the same length and the third longer one. The comparison of the simulated and experimental wavelengths shows the possible agreement for the samples of aspect ratios 2.8 and 3. Hence, we can assume that the rods in the real samples may have one of the studied morphologies. On the other hand, the samples of the aspect ratios 4 and 4.5 possess a different geometry most likely, as the experimental and simulated resonance wavelengths are significantly different. We conclude that for the precise prediction of the optical properties of nanorods, it is necessary to find a suitable model of the nanorod morphology, regarding the aspect ratio, cross-sectional geometry and also truncation at the rod ends, as this effect may also play the role.

Simulation data, provided in the Table 5.2 give the idea of the behavior of the peak FWHM value in an ideal, i.e. uniform sample. The width of the peak increases for the higher aspect ratio. For the real samples, the FWHM increases in tens-nanometer steps, see Table 5.2 and Figures and 5.21 for the comparison. The sample which was found to be the most uniform (AR = 3) has the 2.8 times wider extinction peak than the calculated one. The aspect ratio dispersion, taken as the interval set by the minimum and maximum value of aspect ratio in the Table 5.2, was found to correlate with the width of the experimental peak. As the theoretically predicted broadening with the increasing AR is nearly negligible in comparison to the measured data, we assign the broadening exclusively to the length and width distribution and shape irregularities in the sample. We observed the irregularities in the shape of the rods in the sample with AR = 2.8. The rods seem to be broadened at the endings which may lead to some effects that may also contribute to the width of the spectrum.

AR	min(AR)	max(AR)	Δ AR	Experiment λ_{res} (nm)	FWHM (nm)	Simulation λ_{res}	FWHM (nm)
2.8	2.1	4	1.9	747	201	703	53
3	2.3	3.8	1.5	745	137	725	56
4	3.2	5.3	2.1	764	272	867	58
4.5	3.8	5.8	2	853	253	902	74

Table 5.2: Peak analysis for experimental and theoretical data. The AR value in the first column is the value given by the producer. Minimum and maximum values of aspect ratios were determined from the SEM measurement. The resonance frequency and peak FWHM were obtained by fitting both experimental and DDA-simulated peaks. The simulated peaks were obtained by using the model of rectangular rods.
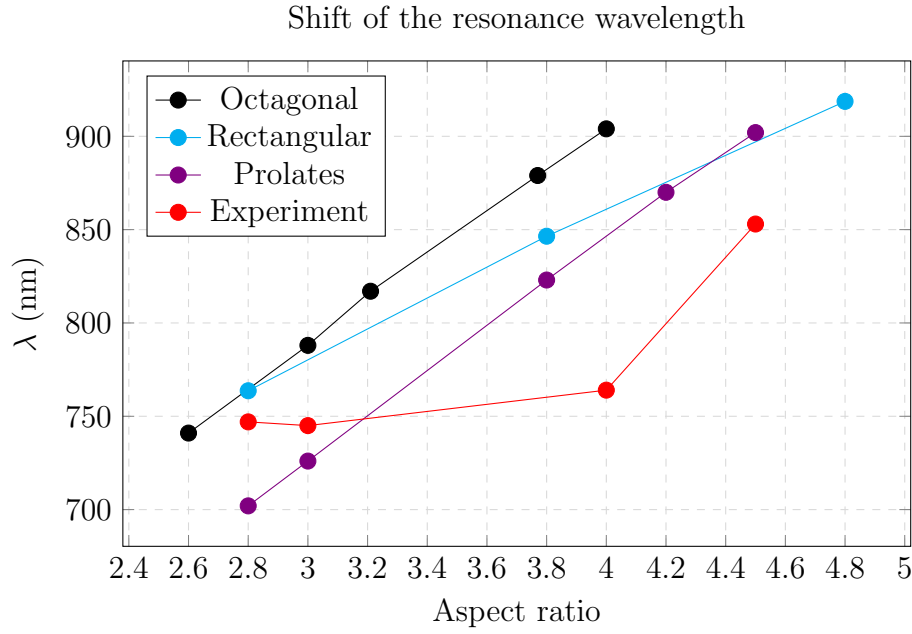
Figure 5.20: Gold nanorods. Dependence of the resonance wavelength for different morphologies of the rod. The resonance wavelength corresponds to the longitudinal plasmon resonancemode. Results calculated by DDA.
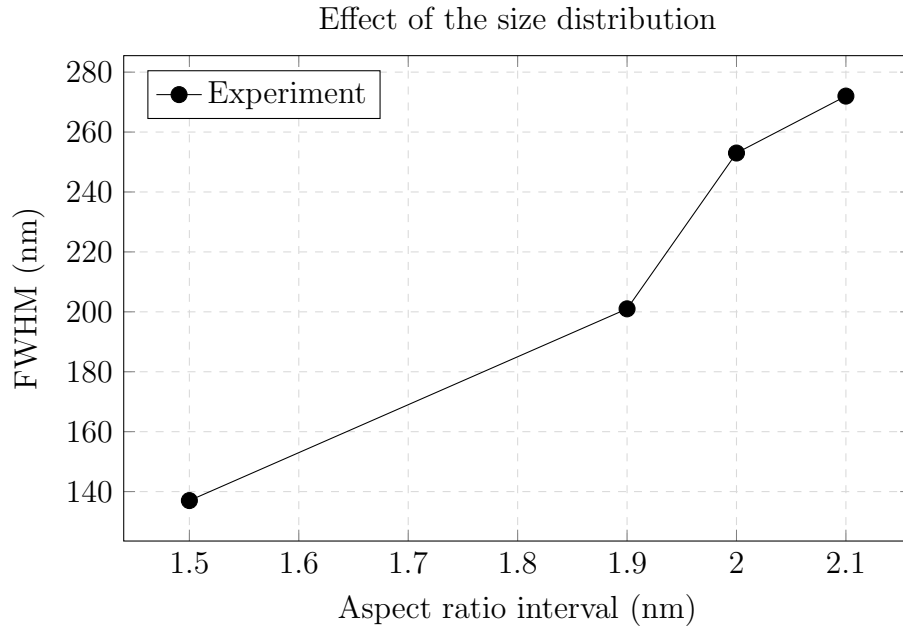

Figure 5.21: Gold nanorods. Dependence of the peak FWHM on the AR dispersion of nanorods in the samples listed in Table 5.2. On the x-axis there is the width of the interval of aspect ratios present in the sample.

Chapter 6

Conclusion

In this work, we have studied optical properties of noble metal nanoparticles. As the optical response of the sample, we have considered the extinction efficiency which represents a quantity accessible by means of theoretical predictions, as well as experiment. Our goal was to validate the measuring process realized on the apparatus assembled for optical spectroscopy experiments, and to investigate reliability of approximative numerical methods in the prediction of the optical properties of coloidal solutions. We have employed the Discrete Dipole Approximation and the Finite-difference Time Domain method.

As the first step, spherical particles have been studied. The Mie solution gives an analytic description of the interaction of spherical objects with light. We have found a very good agreement between the experimental spectra and the Mie solution. Numerical simulations have been found to give an excellent agreement in the range of particle diameters between 20 and 100 nm. For the sizes less than 20 nm, DDA gives the results similar to the Mie solution, whereas FDTD overestimates the resonance wavelength, and its results deviate more. This inaccuracy is probably related to the high sensitivity of the solution to the mesh properties.

In Chapter 5.3, we have focused on the golden nanorods. Simulations have been done by the DDA for the rods in the form of rectangular and octagonal prisms. For the purpose of the spectroscopic measurement, we have obtained the samples with aspect ratios between 2.8 and 4.5. Moreover, one colloidal solution has been synthesized. The comparison of the simulations and experiment has shown a crucial effect of the cross-sectional shape on the shifting of the resonance wavelength. An attempt to quantify the broadening of the main plasmon resonance peak due to the aspect ratio variations has been made.

Finally, we have presented detailed investigation of the optical spectra of silver clusters. Extinction spectra of the equilibrium clusters have been studied, showing a clear dependence of the profile of the spectra on the particle shape. As such results can hardly be reproduced by spectroscopic experiments, the spectra have been transformed into the color map to provide the comparison with the well-known yellow tones of silver colloids.

The presented work has studied the influence of morphology on the behavior of localized surface plasmons. Besides the validation of the measurement technique, the calculated spectra and characterization of golden nanorods represent the step towards the nanoparticle synthesis in the Institute of Physical Engineering at Brno University of Technology with optical spectroscopy as a method for the *in–situ* control of the growth.

Bibliography

[1] Ivan H El-Sayed, Xiaohua Huang, and Mostafa A El-Sayed. Surface plasmon resonance scattering and absorption of anti-egfr antibody conjugated gold nanoparticles in cancer diagnostics: applications in oral cancer. *Nano letters*, 5(5):829–834, 2005.

[2] S Pillai, KR Catchpole, T Trupke, and MA Green. Surface plasmon enhanced silicon solar cells. *Journal of applied physics*, 101:093105, 2007.

[3] KR Catchpole and Albert Polman. Plasmonic solar cells. *Opt. Express*, 16(26):21793–21800, 2008.

[4] John Wang, Julien Polleux, James Lim, and Bruce Dunn. Pseudocapacitive contributions to electrochemical energy storage in tio2 (anatase) nanoparticles. *The Journal of Physical Chemistry C*, 111(40):14925–14931, 2007.

[5] Richard M Crooks, Mingqi Zhao, Li Sun, Victor Chechik, and Lee K Yeung. Dendrimer-encapsulated metal nanoparticles: synthesis, characterization, and applications to catalysis. *Accounts of Chemical Research*, 34(3):181–190, 2001.

[6] L Wang, V Reipa, and J Blasic. Silicon nanoparticles as a luminescent label to dna. *Bioconjugate chemistry*, 15(2):409–412, 2004.

[7] Karen Faulds, W Ewen Smith, and Duncan Graham. Evaluation of surface-enhanced resonance raman scattering for quantitative dna analysis. *Analytical chemistry*, 76(2):412–417, 2004.

[8] Ian Freestone, Nigel Meeks, Margaret Sax, and Catherine Higgitt. The lycurgus cup—a roman nanotechnology. *Gold Bulletin*, 40(4):270–277, 2007.

[9] Gustav Mie. Contributions on the optics of turbid media, particularly colloidal metal solutions (american translation). *Annalen der Physik*, 330(3):377–445, 1908.

[10] M Vrbová. *Lasery a moderní optika - oborová encyklopedie*. Prometheus, 1994.

[11] John William Strutt Rayleigh. On the transmission of light through an atmosphere containing small particles in suspension, and on the origin of the blue of the sky. *The London, Edinburgh, and Dublin Philosophical Magazine and Journal of Science*, 47(287):375–384, 1899.

[12] Craig F Bohren and Donald R Huffman. *Absorption and scattering of light by small particles*. Wiley-Vch, 2008.

BIBLIOGRAPHY

[13] Lianming Tong, Vladimir D Miljkovic, Peter Johansson, and Mikael Käll. Plasmon hybridization reveals the interaction between individual colloidal gold nanoparticles confined in an optical potential well. *Nano letters*, 11(11):4505–4508, 2010.

[14] William A Shurcliff. Polarized light. production and use. *Cambridge, Mass.: Harvard University Press,— c1966*, 1, 1966.

[15] MA Garcia. Surface plasmons in metallic nanoparticles: fundamentals and applications. *Journal of Physics D: Applied Physics*, 44(28):283001, 2011.

[16] Charles Kittel. *Introduction to Solid State Physics*. John Wiley & Sons, 2004.

[17] Petr Dub and Jiří Petráček. *Vybrané problémy z teorie elektromagnetického pole.* VUT Textbook, 2009.

[18] Pedro Lilienfeld. Gustav mie: the person. *Applied optics*, 30(33):4696–4698, 1991.

[19] Cecilia Noguez. Surface plasmons on metal nanoparticles: the influence of shape and physical environment. *The Journal of Physical Chemistry C*, 111(10):3806–3819, 2007.

[20] Andrey B Evlyukhin, Carsten Reinhardt, and Boris N Chichkov. Multipole light scattering by nonspherical nanoparticles in the discrete dipole approximation. *Physical Review B*, 84(23):235429, 2011.

[21] Shoji Asano and Makoto Sato. Light scattering by randomly oriented spheroidal particles. *Applied Optics*, 19(6):962–974, 1980.

[22] John J Bowman, Thomas BA Senior, and Piergiorgio LE Uslenghi. Electromagnetic and acoustic scattering by simple shapes (revised edition). *New York, Hemisphere Publishing Corp., 1987, 747 p. No individual items are abstracted in this volume.*, 1, 1987.

[23] Eduardo A Coronado and George C Schatz. Surface plasmon broadening for arbitrary shape nanoparticles: A geometrical probability approach. *The Journal of chemical physics*, 119:3926, 2003.

[24] Andrea Tao, Prasert Sinsermsuksakul, and Peidong Yang. Polyhedral silver nanocrystals with distinct scattering signatures. *Angewandte Chemie International Edition*, 45(28):4597–4601, 2006.

[25] Jonathan A Scholl, Ai Leen Koh, and Jennifer A Dionne. Quantum plasmon resonances of individual metallic nanoparticles. *Nature*, 483(7390):421–427, 2012.

[26] Kyeong-Seok Lee and Mostafa A El-Sayed. Dependence of the enhanced optical scattering efficiency relative to that of absorption for gold metal nanorods on aspect ratio, size, end-cap shape, and medium refractive index. *The Journal of Physical Chemistry B*, 109(43):20331–20338, 2005.

[27] A Brioude, XC Jiang, and MP Pileni. Optical properties of gold nanorods: Dda simulations supported by experiments. *The Journal of Physical Chemistry B*, 109(27):13138–13142, 2005.

[28] Radek Kalousek, Petr Dub, Lukáš Břínek, and Tomáš Šikola. Response of plasmonic resonant nanorods: an analytical approach to optical antennas. *Optics Express*, 20(16):17916–17927, 2012.

[29] Stephan Link, MB Mohamed, and MA El-Sayed. Simulation of the optical absorption spectra of gold nanorods as a function of their aspect ratio and the effect of the medium dielectric constant. *The Journal of Physical Chemistry B*, 103(16):3073–3077, 1999.

[30] Peter B Johnson and RW Christy. Optical constants of the noble metals. *Physical Review B*, 6(12):4370, 1972.

[31] U Kreibig and L Genzel. Optical absorption of small metallic particles. *Surface Science*, 156:678–700, 1985.

[32] L Sander. Quantum theory of perpendicular electrical conductivity in a thin metallic film. *Journal of Physics and Chemistry of Solids*, 29(2):291–294, 1968.

[33] PM Tomchuk and BP Tomchuk. Optical absorption by small metallic particles. *Journal of Experimental and Theoretical Physics*, 85(2):360–369, 1997.

[34] Anthony Mark Fox. *Optical properties of solids*, volume 3. Oxford university press, 2001.

[35] Lukas Novotny and Niek van Hulst. Antennas for light. *Nature Photonics*, 5(2):83–90, 2011.

[36]

[37] Edward M Purcell and Carlton R Pennypacker. Scattering and absorption of light by nonspherical dielectric grains. *The Astrophysical Journal*, 186:705–714, 1973.

[38] Maxim A Yurkin and Alfons G Hoekstra. The discrete dipole approximation: an overview and recent developments. *Journal of Quantitative Spectroscopy and Radiative Transfer*, 106(1):558–589, 2007.

[39] Bruce T Draine and Piotr J Flatau. User guide for the discrete dipole approximation code ddscat 7.2. *arXiv preprint arXiv:1202.3424*, 2012.

[40] Bruce T Draine and Jeremy Goodman. Beyond clausius-mossotti-wave propagation on a polarizable point lattice and the discrete dipole approximation. *The Astrophysical Journal*, 405:685–697, 1993.

[41] Thomas Wriedt and Ute Comberg. Comparison of computational scattering methods. *J. Quant. Spectrosc. Radiat. Transfer*, 60:411–423, 1998.

[42] Mark L Brongersma and Pieter G Kik. *Surface plasmon nanophotonics*, volume 131. Springer Berlin, 2007.

[43] J Ederth. *Electrical Transport and Ageing in Thin Nanoparticle Gold Films (Licentiate), Uppsala University, 2000*. PhD thesis, Uppsala University, 2000.

BIBLIOGRAPHY

[44] S Shiv Shankar, Suresh Bhargava, Murali Sastry, et al. Synthesis of gold nanospheres and nanotriangles by the turkevich approach. *Journal of nanoscience and nanotechnology*, 5(10):1721–1727, 2005.

[45] Nanfeng Zheng, Jie Fan, and Galen D Stucky. One-step one-phase synthesis of monodisperse noble-metallic nanoparticles and their colloidal crystals. *Journal of the American Chemical Society*, 128(20):6550–6551, 2006.

[46] Xiaohui Ji, Xiangning Song, Jun Li, Yubai Bai, Wensheng Yang, and Xiaogang Peng. Size control of gold nanocrystals in citrate reduction: the third role of citrate. *Journal of the American Chemical Society*, 129(45):13939–13948, 2007.

[47] Scott C Warren, Aaron C Jackson, Zachary D Cater-Cyker, Francis J DiSalvo, and Ulrich Wiesner. Nanoparticle synthesis via the photochemical polythiol process. *Journal of the American Chemical Society*, 129(33):10072–10073, 2007.

[48] Yu-Ying Yu, Ser-Sing Chang, Chien-Liang Lee, and CR Chris Wang. Gold nanorods: electrochemical synthesis and optical properties. *The Journal of Physical Chemistry B*, 101(34):6661–6664, 1997.

[49] Nikhil R Jana, Latha Gearheart, and Catherine J Murphy. Seed-mediated growth approach for shape-controlled synthesis of spheroidal and rod-like gold nanoparticles using a surfactant template. *Advanced Materials*, 13(18):1389, 2001.

[50] Tapan K Sau and Catherine J Murphy. Seeded high yield synthesis of short au nanorods in aqueous solution. *Langmuir*, 20(15):6414–6420, 2004.

[51] Patrick J Straney, Christopher M Andolina, and Jill E Millstone. Seedless initiation as an efficient, sustainable route to anisotropic gold nanoparticles. *Langmuir*, 2013.

[52] Konstantin B Shelimov and Martin Moskovits. Composite nanostructures based on template-grown boron nitride nanotubules. *Chemistry of materials*, 12(1):250–254, 2000.

[53] Catherine J Murphy, Tapan K Sau, Anand M Gole, Christopher J Orendorff, Jinxin Gao, Linfeng Gou, Simona E Hunyadi, and Tan Li. Anisotropic metal nanoparticles: synthesis, assembly, and optical applications. *The Journal of Physical Chemistry B*, 109(29):13857–13870, 2005.

[54] SI Dolgaev, AV Simakin, VV Voronov, GA Shafeev, and F Bozon-Verduraz. Nanoparticles produced by laser ablation of solids in liquid environment. *Applied surface science*, 186(1):546–551, 2002.

[55] Ana L Gonzalez, Cecilia Noguez, and AS Barnard. Map of the structural and optical properties of gold nanoparticles at thermal equilibrium. *The Journal of Physical Chemistry C*, 116(26):14170–14175, 2012.

[56] Tapan K Sau and Catherine J Murphy. Room temperature, high-yield synthesis of multiple shapes of gold nanoparticles in aqueous solution. *Journal of the American Chemical Society*, 126(28):8648–8649, 2004.

[57] Amanda S Barnard and Peter Zapol. A model for the phase stability of arbitrary nanoparticles as a function of size and shape. *The Journal of chemical physics*, 121:4276, 2004.

[58] Günter Wyszecki and Walter Stanley Stiles. *Color science*. Wiley New York, 1982.